ALMA MATER STUDIORUM - UNIVERSITÀ DI BOLOGNA
Dottorato di ricerca in Bioingegneria
Ciclo XXIX
Settore Concorsuale di afferenza: 09/G2
Settore Scientifico disciplinare: ING-INF/06

New segmentation models for the radiologic characterization of polycystic kidney disease patients from MR and CT images

Presentata da: **Dario Turco**

Coordinatore Dottorato
Prof. Elisa Magosso

Controrelatori
Prof. Enrico Caiani
Dott. Giacomo Mori
Prof. Rita Stagni

Relatore
Prof. Cristiana Corsi

Correlatore
Dott. Riccardo Magistroni

Esame finale anno 2017

Relevant abbreviations

ADPKD: autosomal dominant polycystic kidney disease

MRI: magnetic resonance imaging

CT: computed tomography

TKV: total kidney volume

TCV: total cyst volume

Contents

List of Figures

List of Tables

Abstract

Polycystic kidney disease (PKD) refers to a group of inherited disorders characterized by the development and growth of renal cysts. Recent advances in genomics have contributed to a better understanding of the pathogenesis of the disease, suggesting new treatment strategies to inhibit or delay cyst formation and expansion. The efficacy of these therapies is evaluated by estimation of cystic burden measured by magnetic resonange imaging (MRI) as total kidney volume (TKV). TKV is considered to be the best available biomarker of disease progression and for this reason the development of imaging techniques that can provide accurate and reliable quantitative information on the development of renal cyst has become critical.

In this Thesis, different imaging approaches are proposed for a correct characterization of the PKD patient by the estimation of renal and cyst volume from magnetic resonance and computed tomography (CT) images. TKV estimation method from MRI relies on a previously validated method developed for axial images that has been adapted and validated to work on coronal images. The choice of working on coronal images is motivated by the recommendation provided by the Consortium of Renal Imaging Studies in Polycystic Kidney Disease (CRISP) which are followed in several multicenter trials. The results have been compared with the ones obtained from axial images and validated with volume estimation obtained from manual tracing. The performace of the semi-automated method in terms of misclassification of the PKD patient was

also evaluated in comparison with other radiologic approaches currently used for TKV assessment such as the ellipsoid method and the mid-slice method. A novel method for TKV computation from CT images is proposed. This multi-step approach is completely automated and includes preprocessing for data conditioning, localization of the kidneys in the abdomen and the use of a level set approach to identify the renal contour and so extrapolate the renal volume.

The segmented kidneys obtained with the developed methods where used to initialize the segmentation of the cysts. In CT images the total cyst volume (TCV) was obtained using a clustering approach based on the intensity of gray levels. The same strategy was used for MR images with the addition of an extra step to enable cyst counting. Every cyst agglomerate underwent a voting mechanism based on the curvature of the object interface which allowed to distinguish the single cysts. Every cyst is indentified by its centroid that is used for the initialization of a multi-phase level set. The results of this approach for TCV computation was validated through comparison with TCV obtained by manual segmentation.

Nowadays cystic burden is estimated as TKV using methods that rely on geometrical approximation. The proposed automated approaches allow fast and accurate measurement of TKV but also TCV. TCV measurement provide a more precise information on the stage of the disease, opening new paradigms for diagnosis and monitoring of PKD progression.

The last chapter is dedicated to the research activity conducted in the area of diffusion weighted imaging (DWI). DWI is an MRI method for studying Brownian motion of water molecules in tissue, that has shown great potential in differentiating pathological tissue but still has not been explored in ADPKD.

Chapter 1

Introduction

Polycystic kidney disease is a group of inherited disorders identified by the development and growth of cysts in both kidneys that cause progressive renal function loss leading to end-stage renal failure. The most common is autosomal dominant polycystic kidney disease (ADPKD). In recent years, advances in studies on cystogenesis have led to novel targets for the treatment of PKD. Imaging has become an important tool for diagnosis as for monitoring the evolution of the disease and different methods have been proposed during last years. In this chapter are presented the clinical characteristics of ADPKD, the main trials that are exploring the possibility of new clinical targets and the role of imaging as an important tool for diagnosis and prognosis of the disease.

1.1 Autosomal dominant polycystic kidney disease

Autosomal polycystic kidney disease is an inherited, monogenic and multisystemic renal disorder. With an approximated incidence of 1:400 to 1:1000 [2] it is the most common genetic disease [3] and the fourth most common cause

of end-stage renal disease (ESRD) [4]. ADPKD is characterized by the development and the gradual expansion of cysts inside both kidneys (figure 1.1) and is due to the mutation of one of two genes, PKD1 or PKD2. PKD1 is

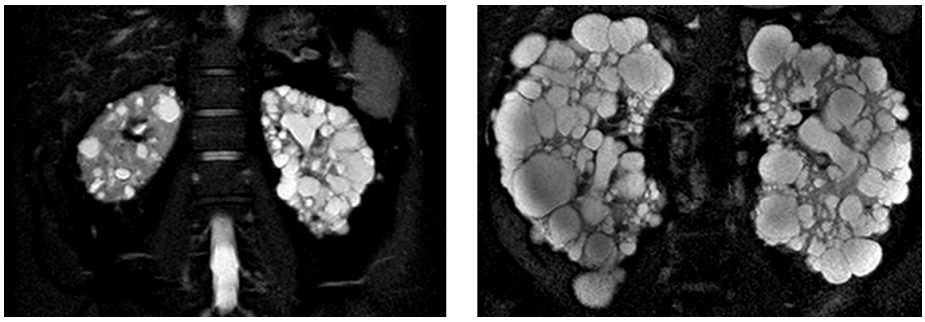

Figure 1.1: T2-weighted images of kidneys in ADPKD patients.

located on chromosome 16p13.3 and encodes polycystin 1 (PC-1), an integral membrane protein with 11 transmembrane domains and a large extracellular structure involved in cell-cell and/or cell-matrix interactions; PKD2 is located on chromosome 4q21 and encodes polycystin 2 (PC-2), a transmembrane glycoprotein that functions as a nonselective cation channel [5, 6]. Mutation in PKD1 gene causes type 1 ADPKD while mutation in PKD2 gene causes type 2 ADPKD. Type 1 ADPKD is the most common and accounts for nearly 85% of cases. It has been noticed that the disease is more severe in patients with PKD1 genotype and that end-stage renal disease develop earlier then in those with PKD2 genotype. ADPKD has a slow lifetime progression and generally patients remain asymptomatic for decades. 50% of the offspring inherite the mutated gene so, in case of absence of family history, early diagnosis of ADPKD is difficult. These fluid-filled cysts, while expanding, compress the kidney vasculature. The progression rate of the disease is related to the position and number of cysts. The most common extrarenal manifestation is polycystic liver disease which is characterized by the development and growth of hepatic cysts leading to liver enlargement. Typical symptoms of polycystic liver disease are related to the liver mass and include dyspnoea, early satiety, gastro- oesophageal re-

flux, and mechanical low-back pain. Other ADPKD's sympthoms can include hypertension, intracranial aneurysms, mitral valve prolapse and acute pain that can be associated with renal haemorrhage, passage of stones, and urinary tract infections [7].

Clinical symptoms usually occur by late middle age and do not provide good indications on the progression of the disease. Furthermore, in the early stage of the disease there is a period of latency in which the renal function, quantified as glomerular filtration rate (GFR) is stable. This is due to the ability of unaffected nephrons for compensating the loss nephrons (figure 1.2) [1]. When most of

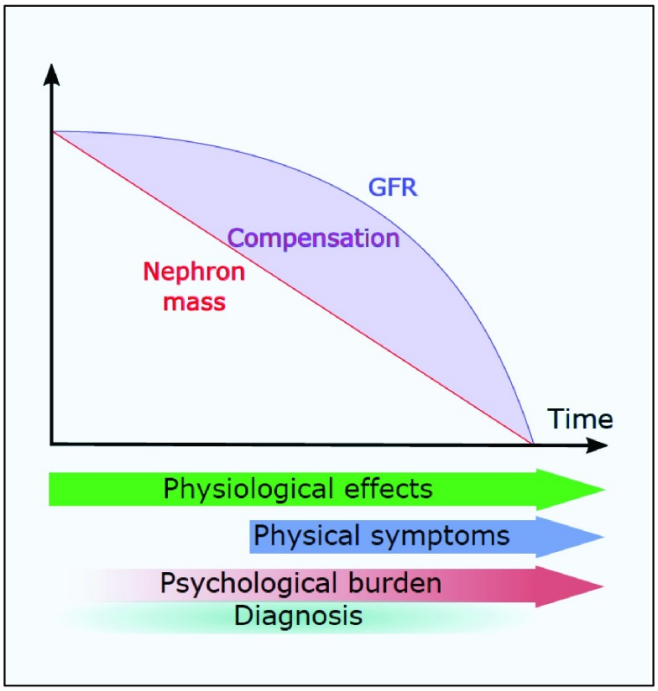

Figure 1.2: The natural history of autosomal dominant polycystic kidney disease as depicted by renal function decline as well as the onset of physical and psychological symptoms [1].

parenchyma turns in cystic and fibrotic tissue, the compensation mechanism

is overwhelmed, GFR decreases substantially and the remaining parenchyma is irreversibly damaged. This has been noticed to happen when at least 50% of functioning parenchyma has been destroyed [8]. For these reasons, GFR, which is the conventional biomarker to evaluate renal function, is not considered useful in PKD evaluation. In order to identify markers of disease progression the Consortium for Radiologic Imaging Studies in Polycystic Kidney Disease (CRISP) was created. According to CRISP, TKV provides an accurate measure of cyst burden and its variation during time is correlated with the decline of GFR. Changes in TKV can be detected in the early stages of the disease so it represents an important biomarker for prognosis as for evaluation of disease progression. Nowadays, cystic burden, measured as total kidney volume, is being established as the best available biomarker of disease progression [9]. Recent prospective longitudinal studies have shown as height-adjusted TKV (htTKV) value of 600 cc/m in adults predicts the onset of renal insufficiency within 8 years. Monitoring cyst espansion has become important to predict outcome or complication of possible therapies; therefore renal imaging plays a crucial role in the diagnosis as in the assessment of the progression of ADPKD.

1.2 Clinical trials and outcomes

Since the identification of PKD1 and PKD2 genes as responsible for ADPKD, a lot of different studies have been undertaken providing new insight into the disease. These studies aim to explore novel therapeutic targets like high dose niacinamide, tyrosine kinase inhibitors and others [10]. The main limitation of these clinical studies is the need of long follow-up, because of the slow progression of the disease and the lack of early sensitive biomarkers. In the next sections will be presented the most recent clinical trials grouped by therapeutic targets.

Blood pressure and the renin-angiotensin system

Hypertension occurs in a majority of the patients while their renal function is still preserved. It is associated to kidney enlargement [11] and contributes to patient morbidity and mortality. It is believed that cyst expansion lead to compression of the vascular tree causing renal ischaemia and activation of the renin-angiotensin aldosterone system (RAAS) [12] and so inhibitors of RAAS such as angiotensin-converting enzyme (ACE), can affect the progression of the disease. In the Halt Progression of Polycystic Kidney Disease (HALT-PKD) clinical trial, ACE inhibition (ACEI) was compared with combined ACEI/angiotensin receptor blockade. Data from HALT-PKD showed that low blow pressure target (<110/75 mm Hg) is associated with a slower enlargement of the kidneys but there was no statistical significance between the estimated GFR and the treatment.

Vasopressin V2 receptor antagonists

Cyclic adenosine-monophosphate (cAMP) activate cyst formation enabling chloride-driven fluid secretion. Studies on animal models demonstrated the effectiveness of vasopressin V2 receptor (V2R) antagonists in the treatment of ADPKD in animal models [13]. Based on these results tolvaptan, a V2R antagonist was tested in ADPKD. The Tolvaptan Efficacy and Safety in Management of Autosomal Dominant Polycystic Kidney Disease and Its Outcomes (TEMPO) 3:4 trial [14] was a 3-year prospective, randomized, double-blinded, controlled clinical trial in adult patients (18-50 years of age) with ADPKD, an estimated creatinine clearance >60 ml/min, a total kidney volume >750 ml and preserved GFR. The administration of tolvaptan in the total TEMPO 3:4 trial population reduced the rate of change kidney volume and was associated with a slower decline of kidney function over 36 months compared to patients on placebo. Adverse events, including hirst, polyuria, nocturia, and polydipsia, were documented

during the treatment and because of this 8% of patients in the treatment group discontinued the trial drug.

Somatostatin analogs

Somatostatin is a peptide inhibitory hormone able to inhibit the generation of intracellular cAMP. The ALADIN trial (A Long-Acting somatostatin on DIsease progression in Nephropathy due to ADPKD) [15] was a prospective, randomised, single-blind, placebo-controlled trial in patients with ADPKD and estimated GFR between 40-15 ml/min/1.73m^2. In this pilot study the potential of somatostatin analogue octreotide in inhibiting the growth of renal cysts was evaluated. The administration of octreotide showed a reduction in the increment of TKV and a slowdown in GFR decline, suggesting that somatostatin analogues can be considered a viable option for long-term treatment of ADPKD. Main limitation of this study was the small sample.
Other trials investigating the potential of somatostatin analogs are ALADIN 2 recruiting 98 patients and the DIPAK 1, involving 300 patients.

Mammalian target of rapamycin (mTOR) inhibitors

Studies on animal models have shown that a drug treatment based on sirolimus, a mammalian target of rapamycin (mTOR) inhibitor can retard cyst expansion. The results of clinical trials in ADPKD patients [16, 17, 18] have been discouraging. Considering the importance of mTOR activation in the pathogenesis of ADPKD the lack of clinical efficacy is probably due to the inability to administer sufficient dosage to achieve biological efficacy [10]. A possible approach to overcome mTOR inhibitor systemic toxicity, while achieving a sufficient level to inhibit mTOR activity in the kidney, could be to target the drug specifically to the kidney [19].

1.3 The role of imaging for the diagnosis of ADPKD

Given the hereditary nature of the disease, genetic testing can be used for ADPKD diagnosis but, due to genetic and allelic heterogeneity, large multi-exon genes, duplication of PKD1, and a high level of unclassified variants it is technical challenging [20]. Because of the high costs and low accuracy (about 80%), the use of genetic testing for diagnosis of ADPKD is limited to the evaluation of kidney donors or in presence of a negative family history.
Diagnosis of ADPKD is tipically based on imaging criteria according to age, family history and number of cysts in individuals. The following diagnostic criteria are used for patients suspected with PKD according to their age [21]:

- For patients aged 15-39 years the presence of 3 or more unilateral or bilateral cysts has a sensitivity of 0.7 and specificity of 1, positive predictive value of 1 and negative predictive value of 0.7.
- For patients aged 40-59 the presence of 2 or more unilateral or bilateral cysts has a sensitivity of 1, specificity of 0.9, positive predictive value of 0.9 and negative predictive value of 1.
- For patients aged 60 years or older the presence of 4 or more cysts in each kidney has a sensitivity of 1 and specificity of 1.

Cysts can be detected using ultrasonography (US), magnetic resonance imaging (MRI) and computed tomography (CT). MRI and CT can provide high resolution images and so have an high sensitivity in detecting even small renal cysts (less than one centimeter in diameter). Due to low cost and no radiation exposure, ultrasound is the modality of choice while MRI is generally used when US is inconclusive.

Ravine's criteria [22] (table 1.1) hass good sensitivity in diagnosis of type 1 ADPKD but showed lower performance in detecting type 2 ADPKD. A unified criteria that allow to overcome this limitation is the one presented by Pei [23] (table 1.2) that shows good sensitivity for both PKD1 and PKD2.

	Number of cysts	
Age (years)	**Positive family history**	**Negative family history**
<30	At least 2 in one or both kidneys	At least 5
30-59	At least 2 in each kidney	At least 5
>60	At least 3 in each kidney	At least 58

Table 1.1: Ravine's criteria for type 1 ADPKD diagnosis.

Age (years)	**Number of cysts**
15-39	Total >3, uni- or bilateral
40-59	Total >4, at least 2 within each kidney
>60	Total >8, at least 4 within each kidney

Table 1.2: Pei's criteria for ultrasonographic diagnosis of ADPKD in patients with positive family history.

Furthermore, presence of liver cysts is tipically observed in 85% of patients by the age of 30 and this information could be used for diagnosis validation especially in absence of a positive family history of ADPKD [24].

In (table 1.3) are summerized the ultrasound diagnostic results for adults with ADPKD obtained with Ravine's and Pei's criteria [25].

1.4 The role of imaging in assessing ADPKD progression

Different studies have shown a link between the progression of cyst growth and renal failure in PKD. It is belived that monitoring cyst volume is helpful for assessing disease progression and evaluating the efficacy of new therapies. Ultrasonography is wildly used for diagnosis of ADPKD but not for the assessment of disease progression because it is highly operator dependent and it has low

	Age range	Subtype	Criteria	Sensitivity (%)
Adult ultrasound diagnostic criteria (Ravine)	15–29	PKD1	$\geq$ 1 cyst	96.2
			$\geq$ 2 cysts	96.2
			$\geq$ 2 cyst in one kidney, $\geq$ 1 cyst in the other	88.5
			$\geq$ 2, bilateral	84.6
			$\geq$ 4 bilateral	80.8
	30–59	PKD1	$\geq$ 1 cyst	100
			$\geq$ 2 cysts	100
			$\geq$ 2 cyst in one kidney, $\geq$ 1 cyst in the other	100
			$\geq$ 2, bilateral	100
			$\geq$ 4 bilateral	100
Adult unified criteria for both PDK1&2 (Pei)	15–29	PKD1	$\geq$ 1 cyst	99.1
		PKD2		79.1
		PKD1	$\geq$ 2 cysts	98.1
		PKD2		71.9
		PKD1	$\geq$ 3 cysts	94.3
		PKD2		69.5
	30–59	PKD1	$\geq$ 2 cysts in each kidney	93.3-92.6
		PKD2		75.8–88.8
		PKD1	$\geq$ 1 cyst	100
		PKD2		96.7–100
		PKD1	$\geq$ 2 cysts	98.2–100
		PKD2		94.9–100
		PKD1	$\geq$ 3 cysts	96.6–100
		PKD2		94.9–95.6

Table 1.3: Ultrasound diagnostic results for adults with ADPKD obtained with Ravine's and Pei's criteria

resolution. The use of US is generally limited to image kidneys of small size. Estimation of total kidney volume from US is generally obtained approximating the kidney shape with an ellipsoid, using the following formula:

$$\pi/6 \cdot length \cdot width \cdot depth$$

where *length*, *width* and *depth* correspond to the principal axes and are manually selected by the operator. Different factors can influence accuracy and reproducibility of this estimates such as the inter operator-variability in detecting the different axes of the ellipsoid, respiratory motion and the non-uniform distribution of cysts that makes the morphology of an ADPKD kidney irregular and far to be considered comparable with an ellipsoid. As a result of these limitations, kidney volume from US obtained applying the ellipsoid formula is underestimated. A study [26] was conducted to evaluate the accuracy of ellipsoid formula in calculating the renal volume from US, comparing the results with the ones obtained using MRI images. The same underestimation occurred applying the formula to MRI images exhibiting the intrinsic inadequacy of this approach. Ultrasounds usually are not taken into consideration for the assessment of disease progression. The first study based on renal volume estimation on ADPKD patients was performed using CT images [27]. Other studies proposed the use of CT for TKV computation suggesting the use of electron-beam or spiral CT in order to increase accuracy in the measurement [28, 29, 30, 31]. Advantages in using CT images for renal volumetric analysis are related to the high resolution of the images that can be also acquired faster than MRI. Disadvantages of CT include ionizing radiation and exposure and, mainly due to the low level of contrast of these images, the use of nephrotoxic contrast agents. Because of these limitations the use of CT in the assessment of disease progression is actually limited. Nowadays MRI is the modality of choice for the assessment of ADPKD progression. The CRISP conducted a prospective, longitudinal study of renal volume progression in patients with ADPKD using T1-weighted and T2-weighted MRI images. Evidence of this study was that kidney volume is the best biomarker for evaluating the rapid progression of the

disease and that MRI is the best technique for its computation. Furthermore it has to be considered that, being the renal enlargement due to cyst expansion, kidney volume is a surrogate biomarker for cyst volume. Because of the high image quality, MRI is the only technique that can allow cyst volume estimation and cyst counting. Different methods have been proposed over the years for kidney and cyst volume estimation in CT and MRI. They will be described in the next chapters.

1.5 Aims of this Thesis

This thesis is focused on the development of new segmentation models for the characterization of ADPKD patient through accurate estimation of renal and cyst volumes. In addition, diffusion imaging analysis is proposed for an early assessment of the disease progression.

Chapter 2

Volumetric analysis in ADPKD patients from MRI

Magnetic resonance is usually the imaging technique of choice in the evaluation of the progression of ADPKD. It is able to image the kidney with an high level of detail and high resolution and because of this it can facilitate the evaluation of the renal volume but also of cyst volume. Furthermore the CRISP defined MRI as the best technique for the volumetric evaluation for the assessment of the rapid progression of the disease. In this chapter are reviewed the recent methods that have been proposed in scientific literature for the volumetric analysis in ADPKD patients from MRI images and will be presented novel approaches for kidney and cyst volume computation.

2.1 State-of-the-art methods

2.1.1 Kidney volume estimation

Mid-slice method

This method refers to the one proposed by Bae [32] for the estimation of kidney volume and may be applicable to MR and CT images. First the mid-slice, defined as the slice positioned in the middle of the image set, is selected. Then, the renal area obtained with manual contouring of this slice is multiplied for the number of slices and for a correction factor of 0.637 for the right kidney and 0.624 for the left kidney. The results obtained by this method have shown good correlation with volumes obtained with manual contouring and better performance in comparison with ellipsoid method. The main limitation is the assumption that a single slice can be representative of the whole kidney. Given the high heterogeneity of polycystic kidneys, this method results to be not suitable for an accurate estimation of kidney volume.

Kidney segmentation during follow-up

In 2015 Kline proposed an automatic method for TKV computation on follow-up MRI [33]. It is based on the registration of the volume detected using stereology on the baseline scan with the follow up scan. The registration is initialized using the image position information obtained from the DICOM header and optimized using inverse warp. The final result is refined using a geodesic active contour model. Good agreement was obtained with manual segmentation results. This method is an important instrument for an accurate estimation of TKV and can require only few minutes for the computation despite 30-40 minutes required for manual tracing or stereology approach. Nonetheless, since the aim is to compute TKV from follow-up, baseline kidneys still have to be manually segmented.

Kidney segmentation with a priori knowledge

In this study [34], the segmentation of the kidneys is achieved using a level set approach. Constraints during the level set evolution are a spatial prior probability map (SPPM) and a propagated shape constraint (PSC). SPPM is obtained using the manual segmentation of the kidneys from a training set of 30 patients. Performance of this fully automated method are good when compared to manual segmentation. Nevertheless, a priori knowledge is needed and, as stated by the author, this method depends strongly from the training set.

2.1.2 Cyst volume estimation

Region-based thresholding

The first method for cyst segmentation was proposed in 2000 by Bae [35].
In each slice an expert radiologist chooses the threshold that allows to better distinguish beetween cysts and parenchyma. Voxel counting is then used for TCV estimation.

Mid-slice method

This method use the same approach used for TKV estimation [32]. First, the mid-slice, defined as the slice positioned in the middle of the image set, is selected. Then, cysts are manually detected and cyst mid-slice area is calculated by pixel count. The cyst volume is obtained multipling the cyst mid-slice area for the number of slices and using a correction coefficient of 0.637 and 0.608 for right and left kidney respectively. As for TKV estimation, the accuracy is affected by how much the mid-slice is representative of the whole kidney.

Shape-detection method

The different steps involved in this method [36] include the use of:

- rough segmentation of the original image through clustering ;
- filtered version of the original image for edge enhancement;
- shape detection level-set to identify a seed point of each cyst in combination with morphological operators;
- morphologic watershed algorithm.

The application of this method is limited to patients with relatively mild to moderate ADPKD as stated in [36], and it is exceedingly complex as stated in an another work from the same group [37].

Euclidean distance map method

To overcome the limitations of the previously presented method [36], the same group proposed a slightly different approach [37].
The workflow of this algorithm includes:

- automatic or manual selection of a threshold;
- connected components analysis to label the cyst regions;
- the construction of an Euclidean distance map;
- watershed segmentation.

2.2 TKV from MRI

CRISP studies evidenced the correlation between renal volume increment and renal function loss and considered MRI as the best tecnique for the computation of TKV and suggested the use of coronal acquisitions.
In a previous work [38] a fast and nearly-automated technique for kidney segmentation was developed. The method was applied to axial images and showed to be able to provide accurate estimation of renal volumes from MRI data. It was tested and validated on patients with ADPKD and normal renal function.

CRISP guidelines recommend the use of coronal images for TKV and TCV measurement. Furthermore, since axial and coronal acquisitions differ from the numbers of acquired planes and resolution, the derived volumes computed applying the disk method to these scans could lead to different estimates.
The mentioned method [38] was applied to images from the coronal view [39]. The aim was to evaluate the differences, if any, between kidney volumes obtained from axial and coronal acquisitions and to compare this approach with the one proposed by the CRISP in [32], in which TKV is based on a limited number of manual area measurements.

2.2.1 Materials and methods

Thirty patients (23 patients with normal renal function and 7 patients with chronic kidney disease) underwent the MRI study. In all patients ADPKD had been previously diagnosed with echographic investigation and based on Ravine's criteria [22]. MRI data were acquired using a 1.5T scanner (Intera Achieva, Philips Medical System). The imaging protocol included unenhanced sequences only. T2-weighted turbo-spin-echo sequences with selective fat suppression (SPIR) respiratory triggered were used to acquire axial images. The kidneys were also imaged posteroanterior in the coronal plane using spectral adiabatic inversion recovery with single shot fast spin echo (SPAIR-SSFSE) with fat saturation. MRI acquisition parameters are presented in table 2.1.

Acquisition parameters	**Axial**	**Coronal**
Spatial resolution (mm)	1.30 x 1.30 to 1.58 x 1.58	0.98 x 0.98
Field of view (cm)	30 to 35	30 to 35
Slice thickness (mm)	5 mm	5 mm

Table 2.1: MRI acquisition parameters

The proposed software was developed to detect kidney contours in both

coronal and axial MR acquisition. The following procedure was applied to both left and right kidneys as shown in figure 2.1

- one point manual selection in the central slice of a volume (a);
- rough segmentation based on Otsu method and region-growing (b);
- morphological operation and curvature motion for final segmentation (c).

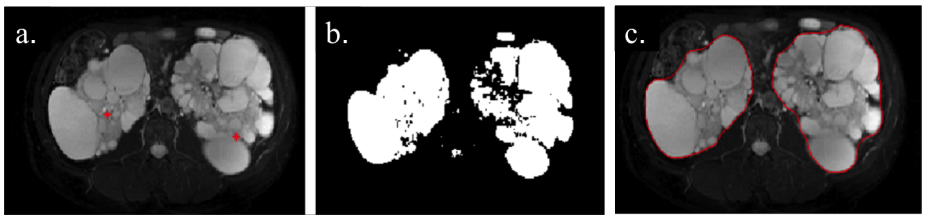

Figure 2.1: Description of the segmentation procedure (from left to right): manual selection of two points in the right and left kidneys (red stars); kidney areas obtained applying a threshold segmentation; kidney contours obtained applying a region growing algorithm and refined by curvature motion.

Starting from the mid-slice, this procedure is iterated forward and backward for each slice in the volume and the seed point automatically recalculated in each plane. Non-kidney structures such as liver or spleen are automatically excluded. In particular the software operates a double check on the left kidney to exclude the spleen. This step is obtained by looking for homogeneous areas in the upper side of the left kidney and comparing the left kidney area of the current slice with the area of the previous one. In case of a larger area and if wide areas of homogeneity are detected, a seed is automatically positioned in the homogeneous area and the result of the application of a region growing algorithm is subtracted to the previous detection (figure 2.2).

For each slice, the kidney area is calculated by counting the number of pixels inside the detected region and considering the data resolution in the acquired plane. Left and right kidney volumes were obtained by summing the products of the corresponding area measurements and the spacing between slices. The

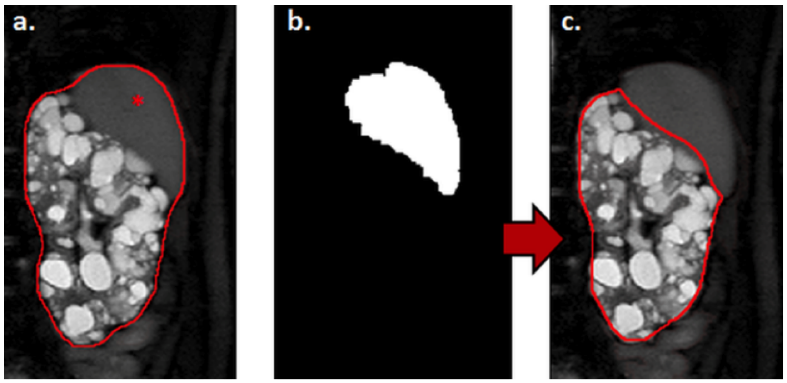

Figure 2.2: Description of the spleen exclusion from segmentation: a. Segmentation result (red contour) and automatically positioned seed (red stars); b. Result obtained applying a region growing based segmentation in the spleen region; c. Final kidney segmentation

software proposed above works indifferently on images from axial and coronal MRI acquisitions to obtain kidney volumes (KVax and KVcor, respectively).

Left and right kidney volumes were also estimated by manual tracing of two independent experts (KVmt) and applying the method described in [32] (KVap). The coronal MR mid-slices of the right and left kidney were manually selected. Mid-slice was defined as the slice whose image number corresponded to a half of the sum of the first and last slice image numbers in the image set. The volume was computed as the product of the mid-slice kidney area and the number of slices covering the kidney and a multiplier derived from the linear best fit model computed for the comparison, as indicated in [32].

2.2.2 Statistical analysis and results

For each patient, kidney volumes obtained from nearly-automated analysis from axial and coronal acquisitions were compared. In addition, the latter ones were also compared with the volume estimates derived by manually tracing of kid-

ney contours and as described in [32]. Comparison was performed using linear regression and Bland-Altman analyses. Paired t-test was applied to verify the significance of the bias.
In addition, to assess the effects of the placement of a single seed point inside the renal cavities kidney (which was the only user input in the analysis), the repeatability of volume measurements was tested in fifteen randomly selected patients in both acquisitions. One observer repeated the analysis twice, selecting two different seed points to compute intra- observer variability. A second observer analyzed the MR data to compute inter-observer variability. The repeatability analysis was also performed to estimate inter-observer variability between volumes derived by manual tracing. Variability measurements were computed as the ratio between the absolute difference between the two volume measurements and their mean value and expressed in percent of their mean.

Two examples of the detected contours in two patients from coronal and axial acquisitions are shown in figure 2.3.

Examples of the segmentation result in one slice for one patient characterized by few cysts and small kidneys and one patient with several cysts and huge kidneys are shown in figure 2.4.

Median value for KVax estimated in 30 patients was equal to 1298 ml (668 ÷ 1973 ml); KVcor resulted in 1298 ml (693-2029 ml) (NS). The same comparison was performed considering right and left kidney volumes separately. Median value for right KVax was equal to 673 ml (321-977 ml) and median value for right KVcor resulted in 651 ml (337-972 ml) (NS). Median left KVax was equal to 614 ml (347-850 ml) and median left KVcor resulted in 617 ml (350- 890 ml) (NS). These ranges reflect the wide variability of the analyzed ADPKD patients.

Linear regression analysis between left KVax and left KVcor (figure 2.5, left top panel, black dots) resulted in an excellent correlation coefficient and regression slope near to 1 (left: KVcor=1.01KVax-2.00; r2=0.996).

Similar results were found for right KV (figure 2.5, right top panel, black

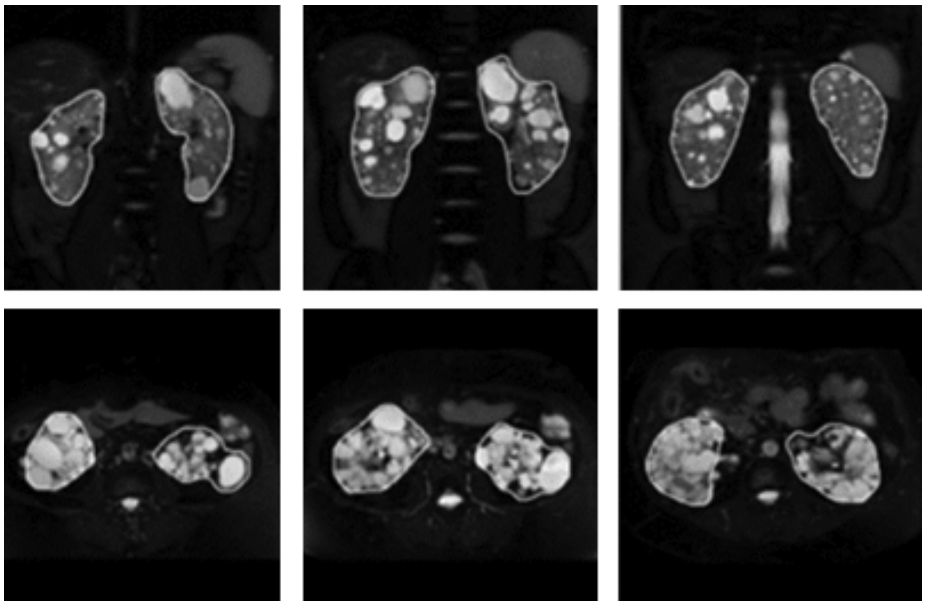

Figure 2.3: Detected contours in two different patients from coronal and axial acquisitions

dots; right: KVcor=1.00KVax+5.30; r2=0.996). Bland-Altman analysis (figure 2.5, bottom panels, black dots) showed a negligible bias between the volume measurements from axial and coronal analysis (bias: -6.7 ml and -5 ml corresponding to -0.9% and -0.7% for left and right KV, respectively). The 95% limits of agreement were relatively narrow (SD: 35.1 ml and 31.5 ml for left and right KV, respectively), providing additional support to the tight agreement between the volume quantification based on axial and coronal acquisitions. Overall, the mean percentage error for the volume assessment in the left and right kidneys resulted in -0.9±6.5% and -0.7±5.5% respectively. In addition, mean absolute percentage error was 5.1±4.0% and 4.0±3.7%.

Linear regression and Bland-Altman analyses (figure 2.6, black dots) between the TKVax and TKVcor confirmed the excellent results obtained for single kidney estimates (y=1.01x-0.78; r2=0.997; bias: -11.7 ml corresponding to -1.5%; SD: 54.3 ml; mean percentage error: - 0.8±4.9%; mean absolute percentage er-

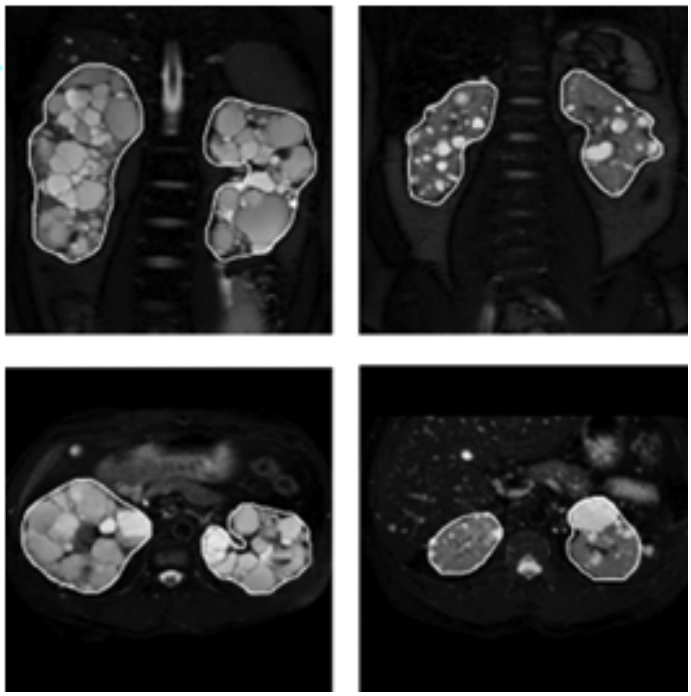

Figure 2.4: Detected contours for one patient with several cysts and huge kidneys (left panels) and one patient characterized by few cysts and small kidneys (right panel).

ror: 4.0±2.8%). Paired t-test between volumes computed analyzing coronal and axial images showed non- significant differences for left, right and total kidney volumes (p¿0.2). Results of the comparison between volumes obtained applying the method proposed in [32] and the nearly-automated method to coronal acquisitions are shown in figure 2.5 (gray dots) for left and right kidney volumes and in figure 2.6 (gray dots) for total kidney volumes.

Quantitative results are summarized in table 2.2.

On a subset of 15 patients, intra- and inter-observer variability in right and left kidney volume measurements obtained applying the nearly-automated method on coronal and axial acquisitions, were 1.8±1.5%, 2.3±1.9%, 1.8±3.1%, 2.5±2.9% and 2.1±2.5%, 1.9±2.3%, 1.8±3.2%, 2.6±4.3%, respectively (figure 2.7).

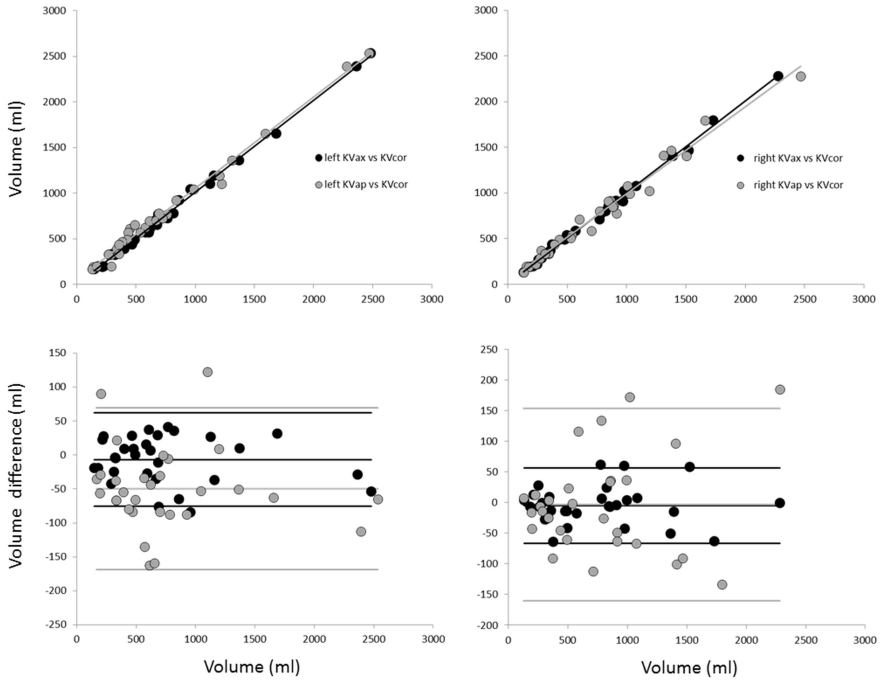

Figure 2.5: Linear regression and Bland-Altman analysis of left (left panels) and right (right panels) kidney volumes.

	regression line	**r**	**bias (ml, (%))**	$SD(ml)$	$\%error$	$\lvert\%error\rvert$
left KVap vs KVcor	y=1.00x+49.37	0.994	-50 (-6.8)	60.8	-10.1±14.1	13.7±10.5
right KVap vs KVcor	y=0.95x+37.54	0.989	-3.7 (-0.5)	81.1	-2.5±10.6	8.7±6.5
total KVap vs KVcor	y=0.98x+75.91	0.995	-53.7 (-7.3)	108.1	-5.8±10.8	9.8±7.3

Table 2.2: TRV results obtained from the analysis of coronal acquisition applying our highly-automated method (KVcor) and the method based on geometric approximations proposed in (KVap).

On note, inter-observer variability computed between the two experts who manually traced the kidney contours on coronal acquisition resulted in 2.6±1.5% and 2.3±1.4% for right and left kidney respectively.

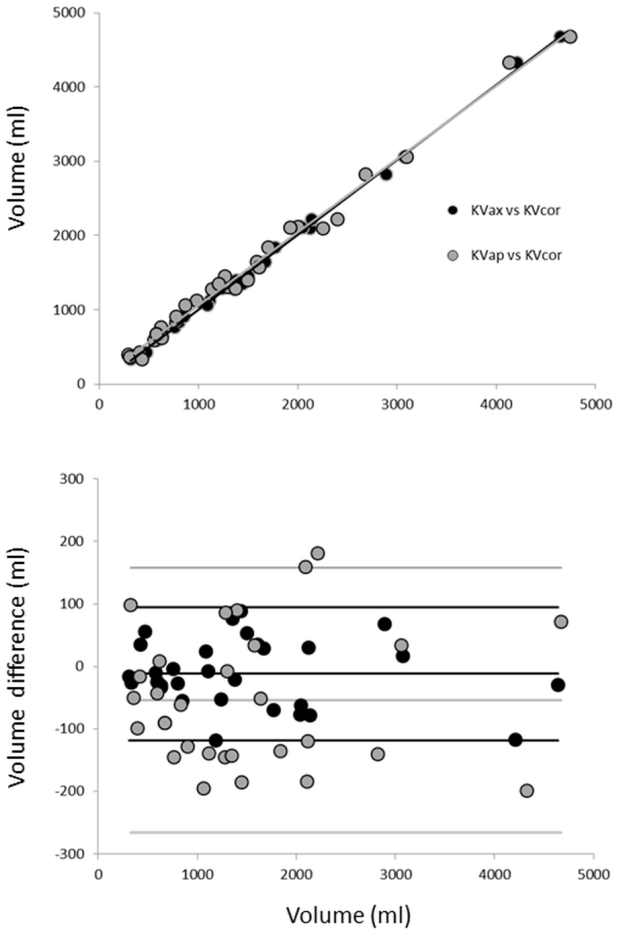

Figure 2.6: Linear regression and Bland-Altman analysis of total kidney volumes.

2.2.3 Discussions

The results showed the method is not tight up to a specific imaging protocol and works when using the CRISP-recommended acquisition protocol and the routine abdominal protocol; therefore, the tool could be valuable in different clinical scenarios when kidneys are imaged for different clinical reasons and the need for renal volume computation is after the fact. The advantage of such

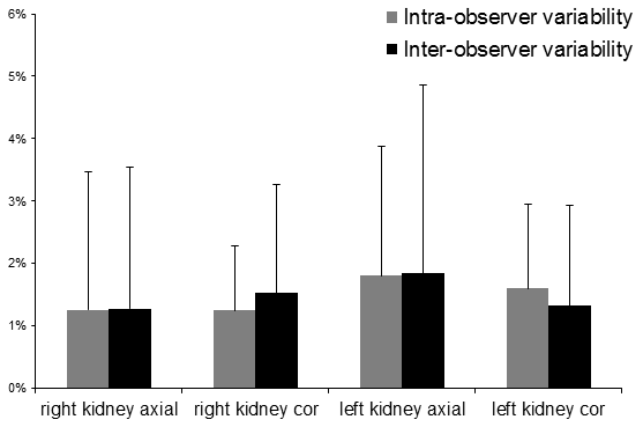

Figure 2.7: Intra- and inter-observer variability in right and left kidney volume measurements on coronal and axial acquisitions

approach relies in the ability to include in our population also patients with huge kidneys. The comparison with kidney volume measurements evaluated using geometric modeling proposed by CRISP [32] showed not negligible bias and large limits of agreement. Both methods perform well on wide range of kidney size and with mild and moderate cystic burden as well as in those in which parenchyma is largely replaced by cysts. However, when kidney shape is not regular and the presence of exophytic cysts or regional morphological variations deform renal contours, volume measurements result inaccurate if evaluated using geometric modeling [32], leading to the large limits of agreement. Two examples in two patients are reported in figure 2.8. In these two cases, the presence of exophytic cysts, not visible in the central plane of the coronal acquisition, result in not negligible errors in left kidney volume estimation applying the geometric modeling based approach. No manual tracing of kidney contours is required for the nearly-automated method and the only manual intervention is the selection of two points inside a single slice of both kidneys whose position was proven not to significantly affect volume estimates by the repeatability analysis. The seeds selected by the user are just an indication of the region to detect and

their position is optimized automatically studying the gray level intensities in a region of interest around the selected points; therefore their initial positions do not affect the final quantitative results. These results were confirmed by intra and inter-observer variability values that resulted very small and negligible for both acquisition views, minor than those computed for manual tracing and those reported in literature applying manual tracing or stereology method [40].
In figure 2.9 is presented the interface developed for kidney segmentation based on this method.

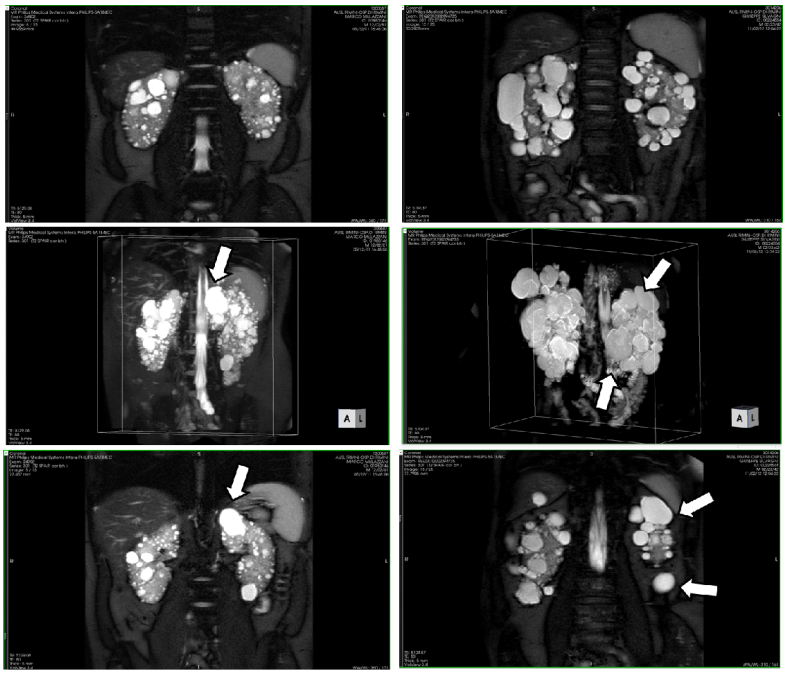

Figure 2.8: Example of the exophytic cysts (indicate by the arrows) erroneously excluded by the segmentation model.

2.3 Patient classification based on TKV

Total kidney volume variation is extensively used in clinical practice to evaluate disease progression and for monitoring treatment efficacy [41]. Height-adjusted

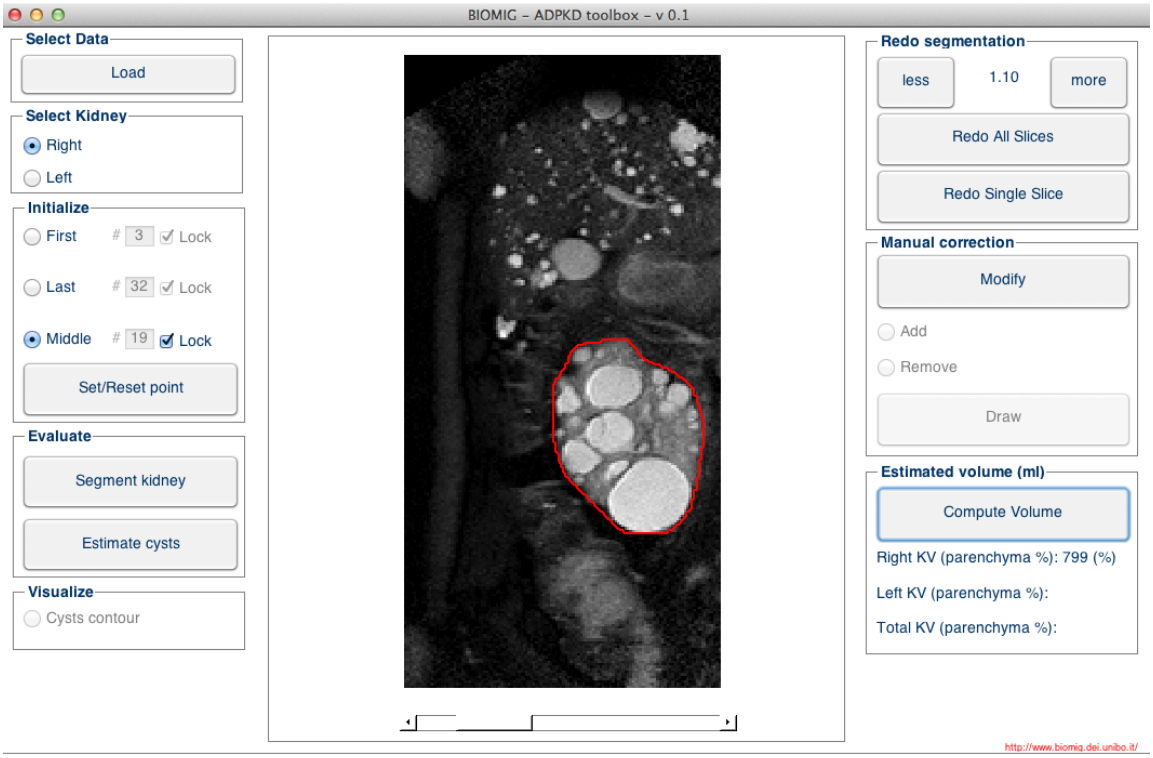

Figure 2.9: User interface for ADPK segmentation

TKV (HtTKV) in combination with age has been also proposed for patient classification which is important for selecting patients for clinical trials [42].
As already reported, different methods have been proposed for computation of TKV in ADPKD patients from MRI. Some of them rely on geometric approximations [32], [42]; others are highly automated [38], [39] requiring a single seed point selection in one mid MR slice to obtain the 3D kidney surfaces and still others [33] and [34], use fully automated approaches. [33] was exclusively proposed to monitor disease progression starting from patient kidney surfaces obtained by manual contouring during first visit; while [34] was based on spatial probability density maps and regional mapping with total variation regularization and propagated shape constraints.

In the next section a study conducted to perform a quantitative comparison

of the performance of the available methods for TKV computation is described. Two methods based on geometric assumptions (mid-slice, ellipsoid) and a third one on true contour detection were tested on forty ADPKD patients at different disease stage using MRI. Ellipsoid method was also tested using ultrasound images in a subset of fourteen patients. Their performance was compared versus TKVs derived from reference manual segmentation of MR images. Aim of this study is to evaluate if differences in TKV can lead to different prognostic classification [42].

2.3.1 Materials and methods

Forty patients were enrolled in this study. In all the patients ADPKD was diagnosed based on the Ultrasonographic Unified Criteria [23] and MR images were acquired following the acquisition protocol described in [43]. In a subset of fourteen patients ultrasound images were available. Patients characteristics are reported in table 2.3.
TKV was estimated using the ellipsoid method [42], the mid-slice approach [32] and the highly-automated method described in the previous section.

Characteristics	**Value**
Number of patients	40
Sex (M/F)(%)	56,4/43,6
Age at visit (years) Mean [range]	44 [21-66]
Creatinine (mg/dl) Mean [range]	1,37 [0,6-2,13]
GFR (CKD-EPI ml/min/1.73 m2) Mean [range]	73,8 [32-131]
Number of patients treated with one anti-hypertensive drug	8
Number of patients treated with two anti-hypertensive drugs	4
Number of patients treated with at least 3 anti-hypertensive drugs	5

Table 2.3: Patients characteristics.

2.3.2 Statistical analysis and results

To evaluate the agreement between TKVs computed applying the reference technique, based on manual segmentation of MR images, and the different approaches, regression and Bland-Altman analyses were performed. Intra-class correlation coefficients (ICC) and absolute errors were also computed for each technique. Dice coefficient was computed for the methods in which kidney surfaces were available. In 20 patients randomly selected, kidney volumes from MRI were computed twice by two reviewers, blinded to their previous results. Based on computed TKVs, patient classification was assessed [42] and results were compared with classification obtained using TKV from manual tracing.

Median volumes characterizing our analysis are reported in table 2.4.

	Manual tracing MRI (40 patients)	**EL MRI (40 patients)**	**MS MRI (40 patients)**	**AUTO MRI (40 patients)**	**EL Echography (14 patients)**
Median right KV (ml)	645 [IQR: 446÷1118]	747 [IQR: 416÷1097]	627** [IQR: 407÷1069]	639 [IQR: 448÷1104]	426* [IQR: 258÷776]
Median left KV (ml)	657 [IQR: 502÷1539]	705 [IQR: 487÷1484]	673 [IQR: 476÷1589]	645 [IQR: 510÷1505]	462* [IQR: 342÷885]
Median TKV (ml)	1383 [IQR: 916÷2673]	1444 [IQR: 905÷2714]	1300** [IQR: 887÷2559]	1358 [IQR: 943÷2593]	881* [IQR: 657÷1660]

Table 2.4: AUTO = highly-automated method, EL = ellipsoid method, IQR = interquartile ranges (25%÷75%), KV = kidney volume, MS = mid-slice method, *$p<0.05$ vs reference value by manual tracing, **$p<0.01$ vs reference value by manual tracing.

Kidney volume		**ICC**	95 % CI [min ÷ max]
KV_{EL} (n=40)	Right	0.977 (p<0.001)	0.956 ÷ 0.988
	Left	0.977 (p<0.001)	0.957 ÷ 0.988
	Total	0.983 (p<0001)	0.967 ÷ 0.991
KV_{MS} (n=40)	Right	0.984 (p<0.001)	0.970 ÷ 0.992
	Left	0.987 (p<0.001)	0.975 ÷ 0.993
	Total	0.992 (p<0.001)	0.985 ÷ 0.996
KV_{AUTO} (n=40)	Right	0.999 (p<0.001)	0.998 ÷ 0.999
	Left	0.997 (p<0.001)	0.995 ÷ 0.999
	Total	0.999 (p<0.001)	0.997 ÷ 0.999
KV_{ECHO} (n=40)	Right	0.862 (p<0.001)	0.635 ÷ 0.953
	Left	0.864 (p<0.001)	0.550 ÷ 0.953
	Total	0.843 (p<0.001)	0.592 ÷ 0.946

Table 2.5: 95% CI = 95% confidence intervals, ICC = Intra-class correlation coefficients, KV_{AUTO} = kidney volume by the highly-automated method, KV_{echo}= kidney volume by echography, KV_{EL} = kidney volume by the ellipsoid method, KV_{MS} = kidney volume by the mid-slice method.

Linear regression (figure 2.10, left panels) and Bland-Altman (figure 2.10, right panels) analyses between kidney volumes estimates obtained applying the three approaches based on MRI (MS, EL and AUTO) and echography versus reference kidney volumes by manual tracing are shown in figure 2.10 for right, left and total kidney volume respectively. The intra-class correlation coefficients for TKV are reported in table 2.5.

We found a mean Dice coefficient of 0.98±0.02 and 0.97±0.02 for right and left kidney respectively applying the highly automated method. Patient classification according to the Mayo Clinic calculator [3] showed the following misclassification: 5/40 (13%), 4/40 (10%), 1/40 (2.5%) using TKVs obtained applying the ellipsoid, the mid-slice and the highly automated method, respectively. Im-

portantly, in 14 patients in which echographic quantification was available, only 3 patients (21%) were correctly classified; in general, US-based classification resulted in the assignment of the patient to a class associated to a lower kidney growth rate.

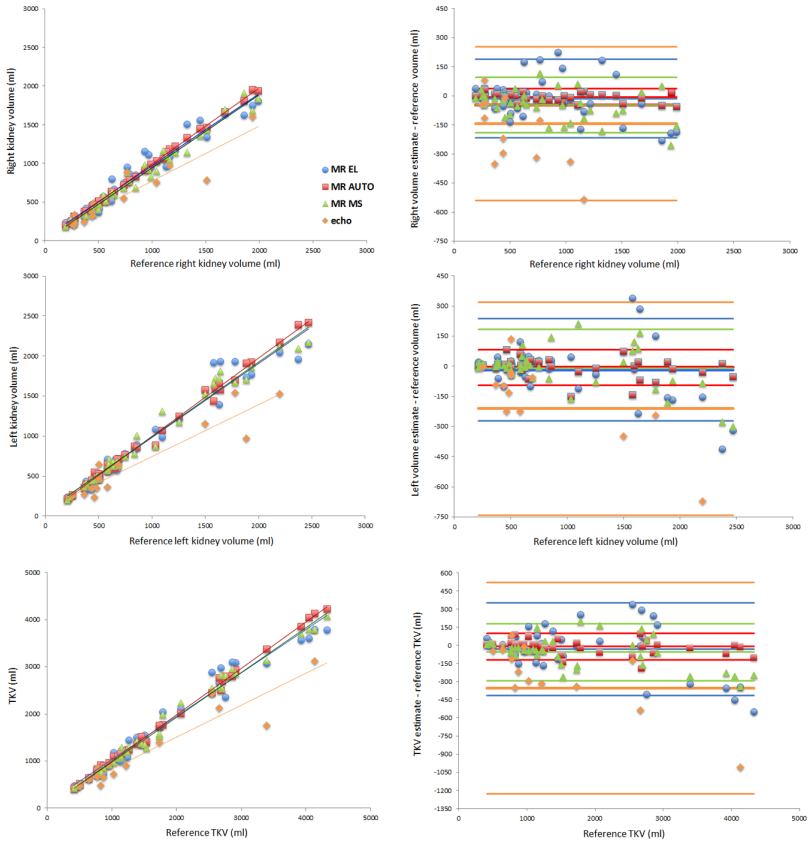

Figure 2.10: Linear regression (left panels) and Bland-Altman analysis (right panels) for right (top panels), left (mid panels) and both kidneys (bottom panels) volumes applying the highly-automated (AUTO, red squares), ellipsoid (EL, light blue diamonds) and mid-slice (MS, green triangles) methods to MR images and the ellipsoid approximation to echographic images (dark yellow diamonds).

2.3.3 Discussions

Different approaches for TKV computation were compared in the same group of ADPKD patients at different disease stage characterized by a wide renal volume range. The MRI-based methods resulted in excellent correlation coefficients and ICCs. However, Bland- Altman analysis showed underestimation of different magnitude for the three techniques. Limits of agreement were highly dependent from the applied method, showing the best agreement for the highly automated technique (<5%); they were large for the EL method, resulting in confidence intervals larger than 10%. Mean percentage errors confirmed these results showing errors <1% for the highly automated technique. Importantly both geometrical-based approaches show an increased volume underestimation for both kidney volumes when kidney size increases. In addition, variability analysis results exhibit that ellipsoid and mid-slice methods are highly operator-dependent showing statistically different TKV estimates for both intra and inter-observer variability. Overall, the best performance was obtained applying the highly automated method. The results of this comparison are in line with the ones previously presented [42, 39, 32]. Slight differences were found for variability analysis that could be explained by considering the population selected for this analysis is characterized by huge kidneys. In a previous study [44] sonographic assessment of TKV by applying the ellipsoid method was compared versus TKV derived from MRI. Results showed inaccurate ultrasound-based TKV estimates and, differently from what we found, sonographic volumes were greater than MRI-based TKV. However, authors state renal volume was exaggerated in the aggregate, but volume was also undermeasured in many kidneys. The error was not related to kidney size or body habitus, suggesting that is not caused by patient-specific factors, but much of the variability was related to the sonographers. In addition, in this study, T1-weighted MR images were used to derive TKV by stereology. A direct quantitative comparison with the method presented in [34] was not possible since specific algorithm was not available. The method in [34] was tested on a population of smaller kidneys (TKV

range: 177÷2634, mean TKV: 885±570) and validated versus manual tracing. Compared to the highly automated method, linear regression coefficient and ICC were slightly minor (r=0.97, ICC=0.97). Importantly computed bias was between 25 and 30 ml (about 3.5%) but limits of agreement were huge (57 ml vs 266 ml and 290 ml) compared to the ones obtained by the highly automated method. Dice coefficient was also slightly lower (0.88±0.08) in [34]. Regarding classification, a correct patient clustering is crucial to select patients who are appropriate for clinical trials or, more importantly, likely to benefit from an effective treatment. Differently from [45], our results showed techniques based on geometric models, both from echography and MRI, are not suitable for an accurate patient stratification based on renal volume. Previous study [26] already showed poor accuracy and reproducibility of ultrasound for TKV assessment using the ellipsoid formula; however the use of TKV from echography applying geometric models has been recently proposed as a prognostic index in ADPKD population [46]. In [46], simultaneous ultrasound and magnetic resonance imaging were used to determine whether ultrasound and kidney length predict future chronic kidney disease stage 3 over 8 year follow-up. Results showed they are equivalent for this purpose. This comparison is beyond the aim of this technical note in which kidney length was not considered and the focus was on volumetric information. However our preliminary results show an extremely low accuracy of kidney estimation obtained from echographic exam and echo-derived measurements lead to inaccurate patient stratification in the majority of patients. Our study suggests that ultrasound prognostic estimation should be used with extreme caution, and final clinical validation of this approach would require further confirmation from independent studies. To conclude, approaches based on image processing techniques [39, 38, 34] which already proved to provide good results and could be ready for clinical testing, should be taken into account for kidney volume quantification and monitoring. Importantly, differently from ellipsoid and mid-slice methods, these approaches make available a 3D model of the kidneys that could be very useful for further analysis including cyst detection, cyst volume computation and automatic classification of renal morphology

(e.g. class 1 versus class 2 kidneys [42]).

2.4 TCV from MRI

TKV is widely considered as the best prognostic biomarker for the assessment of renal function failure. However, kidney enlargement in ADPKD patients is due to cyst expansion. The mechanisms beyond the formation and the growth of cysts are still unknown but the estimation of cyst volume is a critical parameter for the evaluation of the progression of the disease. The prognostic value of TKV as surrogate biomarker for TCV can fail in predicting change in renal function, as, for example, in patients with few large cysts or in patients with renal atrophy secondary to ischemia or urinary tract obstruction [47]. As already stated, a correct classification of an ADPKD patient is important for the evaluation of therapy efficacy as for the enrollement of patients in clinical trials. In this section a novel approach for fully automated cyst segmentation is presented.

2.4.1 Materials and methods

Algorithm for TCV assessment was tested in five patients. For all patients ADPKD diagnostic was based on the Ultrasonographic Unified Criteria [23] and MR images were acquired following the acquisition protocol described in [43]. Segmentation of the kidneys was obtained using the validated method described in [39] and used to mask the original data.

For each image in the MR dataset, the following procedure was designed. The following procedure includes

- cyst detection
- seed detection
- cyst segmentation

Cyst detection

A 3-class fuzzy c-means clustering was applied to every single image in order to distinguish cystic from parenchymal regions. Fuzzy clustering resulted in a powerful unsupervised method for the analysis of this kind of data, allowing to obtain quick estimation of TCV. Later on in the manuscript, the results of TCV estimation will be presented and discussed. An example of the clustering result is shown in figure 2.11

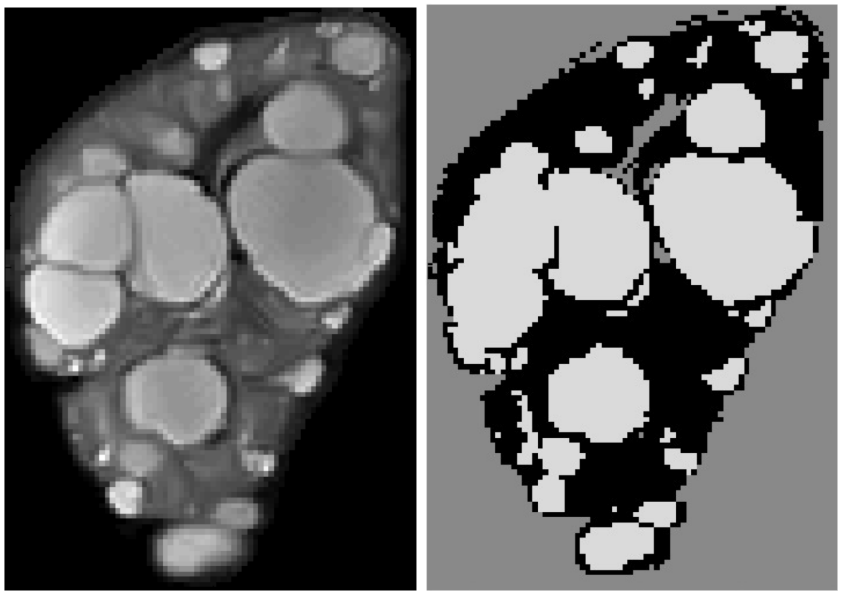

(a) Original image with kidney segmentation mask

(b) Cyst detection by 3-class clustering

Figure 2.11: Result from the clustering of a segmented kidney

Seed detection

This clustering results in the detection of different regions that can be associated to a single or multiple cysts. Only regions with an area bigger than twice the

slice thickness are taken in consideration for this kind of analysis since the aim is to distinguish every single cyst and estimate its volume. The iterative voting approach used for the detection of single cysts is based on the consideration that cyst expansion occurs radially without a preferential direction and can be modelled by a sphere. In a more general scenario cyst expansion is conditioned by the presence of other cysts resulting in an agglomerate. These regions, detected by the clustering approach previously described, are convex and often radially symetric.

In this section will be described the iterative radial voting approach [48] used to locate the centroid of each cyst.

Let $I(x, y)$ be the original image where (x, y) are the spatial coordinates of a point in the image domain, $\nabla I(x, y)$ the image gradient, $\|\nabla I(x, y)\|$ the magnitude of the image gradient and $\alpha(x, y) := (\cos(\theta(x, y)), \sin(\theta(x, y)))$ be the voting direction at each point of the image for some angle $\theta(x, y)$ that varies with the image location and is the angle of the gradient direction respect to x axis. Defining a subset of pixels $S := \{(x, y) | \|\nabla I(x, y)\| > \Gamma_g\}$ where Γ_g is the gradient threshold and considering that in the binary mask resulting from the clustering, the background pixels are set to zero, for each point $(x, y) \in S$ the voting direction can be defined as the negative gradient direction:

$$\alpha(x, y) := -\frac{\nabla I(x, y)}{\|\nabla I(x, y)\|}.$$

Being the centroid of a cyst far away from its boundary, in order to reduce the number of calculations, for each point $(x, y) \in S$ is defined a cone shape voting area $A(x, y; r_{min}, r_{max}, \Delta)$ dependent on the radial range r_{min}, r_{max} and on the angular range Δ.

$$A(x, y; r_{min}, r_{max}, \Delta) := \{(x \pm r\cos\phi,\ y \pm r\sin\phi) \,|\, r_{min} \leq r \leq r_{max} \quad and \\ \theta(x, y) - \Delta(x, y) \leq \phi \leq \theta(x, y) + \Delta(x, y)\}$$

In the center of the voting area is defined a 2D Gaussian kernel $g(x, y, \sigma)$ as

follow

$$g(x, y, \sigma) = \frac{1}{\sqrt{2\pi\sigma}} exp\left(-\frac{(x^2 + y^2)}{2\sigma^2}\right)$$

with variance σ^2. The voting area so defined is illustrated in figure 2.12.

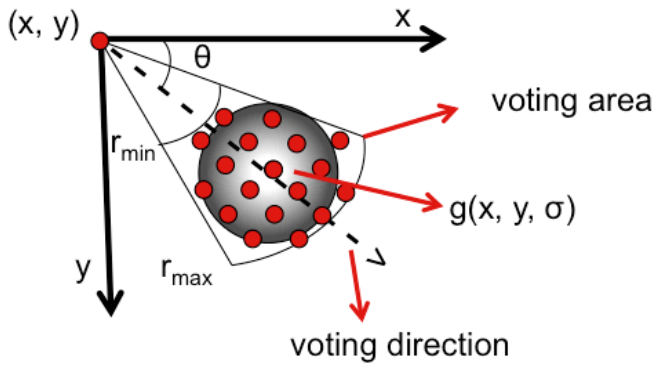

Figure 2.12: Cone shape voting area with Gaussian kernel positioned in its center.

Each pixel of the object interface contributes to a vote image that has the same size of the original image, is initialized to zero and defined as:

$$V(x, y; r_{min}, r_{max}, \Delta) = \sum_{(u,v) \in A(x,y;r_{min},r_{max},\Delta)} \{F(x, y)g(u, v, \sigma)\}$$

where the feature image $F(x, y)$ is the local external force at each pixel of the original image. In this study, as external force, it has been choosen the mean curvature k defined as:

$$k(x, y) = \nabla \cdot \left(\frac{\nabla I(x, y)}{|\nabla I(x, y)|}\right)$$

In order to reduce the computational weight and so to increase efficiency, differently by [49], here it has been used a single pass approach similarly to [48] to locate the seeds for the next step. The centroids of the detected objects are detected selecting the local maxima of the resulting voting image (V).

An example of the intermediate steps to achieve the detection of the centroid on a synthetic image is shown in figure 2.13 (central panels).

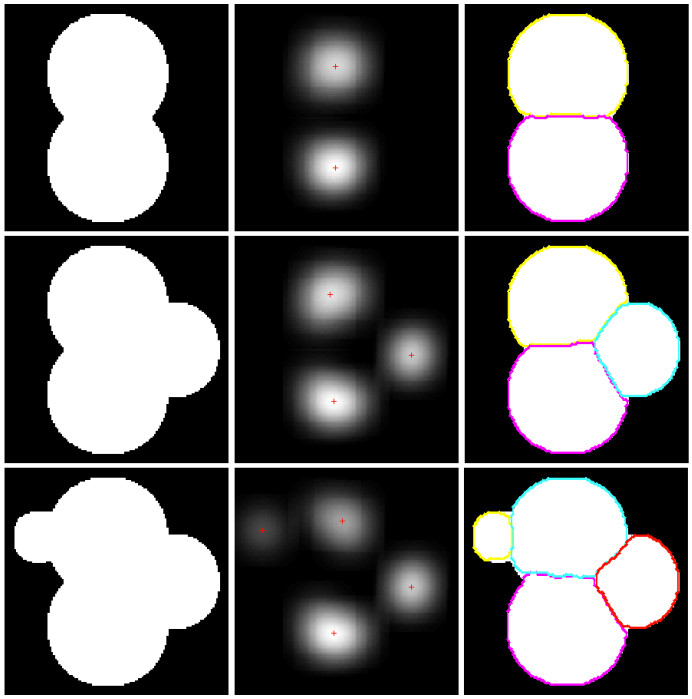

Figure 2.13: Examples of the segmentation of touching objects on synthetic images: test images (left panels); seed detection (central panels); result of segmentation (right panels).

Cyst segmentation

The detected centroids are used as seeds for the segmentation of cysts that has been obtained using a level set approach based on interactive model. The mechanism involved in the interaction are a repulsion term for separating the touching cysts and preventing the contours from overlapping and a competition term for defining the boundaries and to determine the membership of each pixel. Let be $C_i(i = 1, ..., N)$ where N is the number of detected cysts (centroids) for the considered clustered object. Each cysts is represented by its own level set

energy function Ψ_i with C_i as the zero level set such as $C_i = \{(x,y)|\Psi_i(x,y) = 0\}$. In the multiphase level set approach each level set (Ψ_i) interacts with the others through the repulsion and competion terms. The evolution of each curve is obtained by the minimization of the energy function and can be expressed as

$$\frac{\partial \Psi_i}{\partial t} = \delta(\Psi_i)\{\lambda_o|I - c_i|^2 - \lambda_b|I - c_b|^2 \prod_{j=1, j\neq i}^{N} H(\Psi_j) + \dots$$
$$\mu\nabla g\frac{\nabla\Psi_i}{|\nabla\Psi_i|} + \gamma g\nabla\cdot\Big(\frac{\nabla\Psi_i}{|\nabla\Psi_i||}\Big) + \omega\sum_{j=1, j\neq i}^{M}(1 - H(\Psi_j))\} \tag{2.1}$$

where g is the edge indicator, H is the Heaviside function, δ the Dirac function and λ_o, λ_b, μ are parameters of the equation.

Examples of the final segmentation through the multiphase level set approach of a synthetic image is shown in figure 2.13 (right panels).

Cyst counting

As previously mentioned, only regions with an area bigger than twice the slice thickness underwent the based on the multiphase segmentation approach. Seed detection is a crucial step and an erroneous in the detection of the centroid of the regions can lead to over- or under- segmentation of the agglomerate of cysts. The developed approach for cyst counting allows to detect the number of cysts in the kidney using the position of the centroids of each segmented object.
The different 2D segmented objects are associated to a single 3D object (a cyst) depending of the closeness of their centroids in the third dimension and the percentage of overlap between them. The redundancy of these informations along the third dimension allows also to overcome the limitation of the method for seed detection.

2.4.2 Statistical analysis and results

An example of the result of the previosly described workflow on an agglomerate of cysts is shown in figure 2.14. Two expert radiologist manually traced the

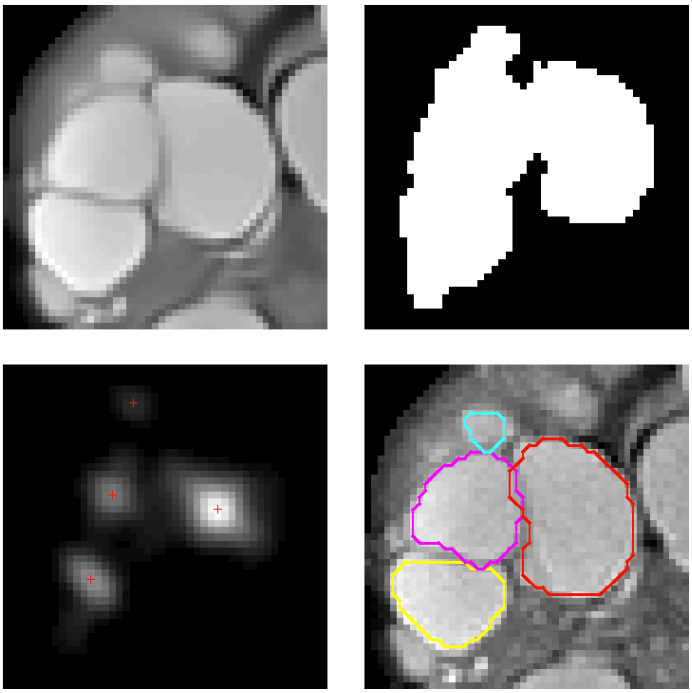

Figure 2.14: Intermediate steps of the segmentation algorithm: original image (top left); agglomerate of cysts detected through clustering (top right); detection of cyst centroids (bottom left); result of the segmentation (bottom right).

cysts in both kidneys of each of the five patients providing two estimations of the volume of the cysts. Cyst volume obtained from the automatic method was compared with the mean of the two manual estimated cyst volumes. Comparison was performed using linear regression and Bland-Altman analyses, figure 2.15. Linear regression resulted in an excellent correlation coefficient and regression slope near to 1 (y=1.00x-0.89; r=0.987).

Bland-Altman analysis showed a moderate bias (bias: -0.26 ml corresponding

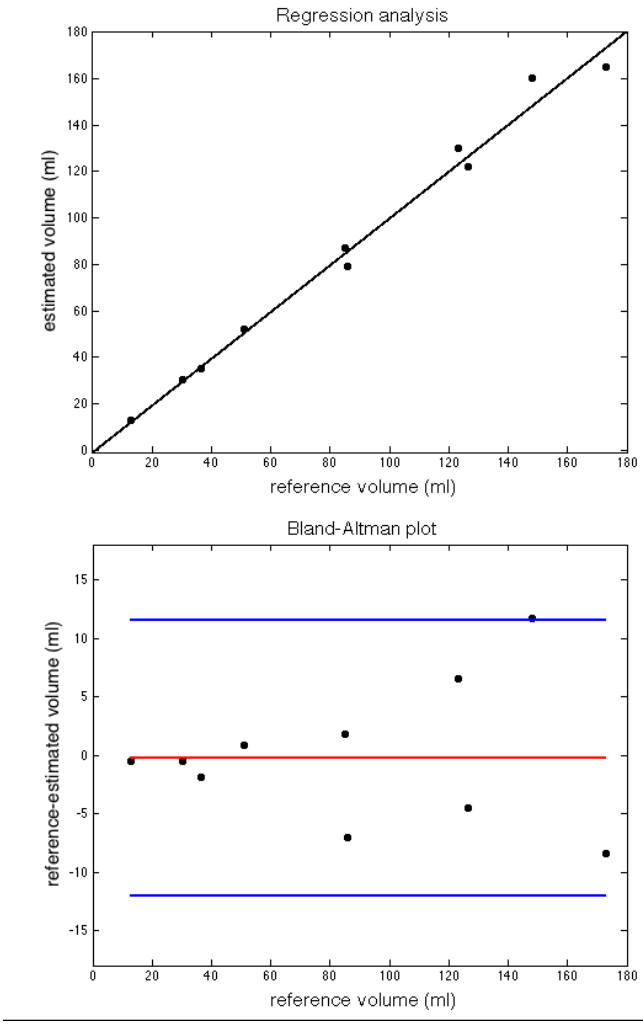

Figure 2.15: Linear regression and Bland-Altman analyses of TCV

to -0.30%).

The 95% limits of agreement resulted in 6.03 ml, mean percentage error was -1.1 ± 5.1% and mean absolute percentage error was 4.5±2.3%.

Residual parenchyma percentage was computed using the estimated CV from the KV (table 2.6).

	Patient ID	**TKV (ml)**	**TCV ME1 (ml)**	**TCV ME2 (ml)**	**Mean ± std (ME1 vs ME2) (ml)**	**TCV AE (ml)**	**Error (%)**	**Residual parenchyma (%)**	**Cyst (%)**
Right kidney	1	239.65	78,58	93,34	85.96 ± 10.44	78.90	-8.22	67.08	32.92
	2	365,47	48,92	53,53	51.22 ± 3.26	52.01	1.53	85.77	14.23
	3	350.57	117,44	135,64	126.54 ± 12.87	121.96	-3.62	65.21	34.79
	4	208.59	29,82	31,45	30.60 ± 1.15	30.03	-1.97	85.60	14.40
	5	447.91	137,44	159,38	148,41 ± 15.51	160.07	7.86	64.26	35.74
Left kidney	1	230.94	36,11	37,53	36.82 ± 1.00	34.91	-5.18	84.88	15.12
	2	486.73	76,30	94,02	85.16 ± 12.53	86.87	2.00	82.15	17.85
	3	377.68	165,77	180,48	173.13 ± 10.40	164.65	-4.89	56.40	43.60
	4	179.83	14,17	12,22	13.19 ± 1.38	12.57	-4.72	93.01	6.99
	5	454.8	114,63	131,79	123.21 ± 12.13	129.65	5.23	71.49	28.51

Table 2.6: TCV and parenchyma estimation. ME1: Manual estimation #1; ME2: Manual estimation #2; AE: Automatic estimation;

Cyst counting allowed to obtain the volume of each cyst and so to quantify the contribution of each single cyst to the total cyst volume. In table 2.7 is shown the volume of the five biggest cysts for each kidney that has been analyzed.

An example of the segmented cystic burden is shown in figure 2.16.

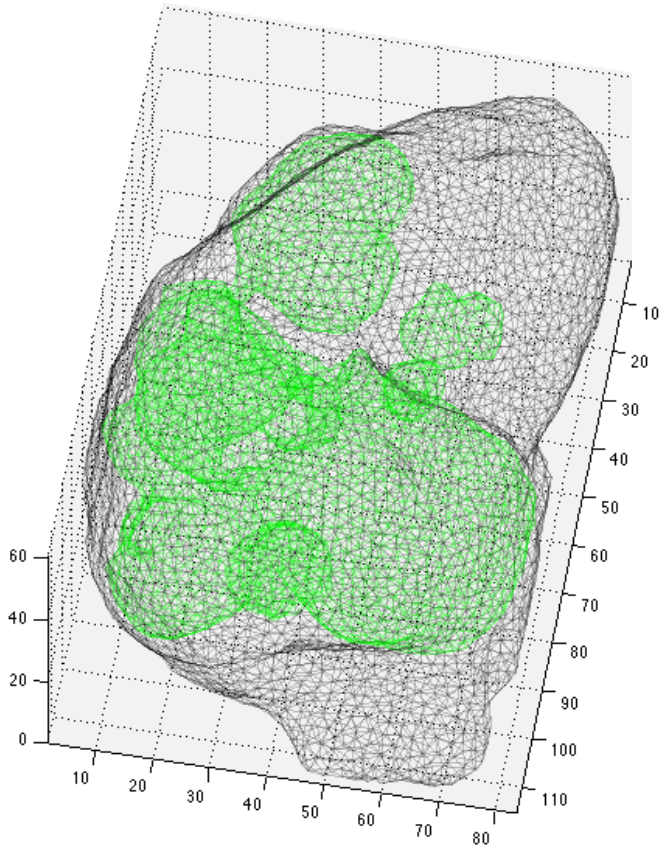

Figure 2.16: Example of the segmented cyst volume (green), right kidney, patient 3.

In figure 2.17 are shown the three biggest cysts in each kidney volume.

	Patient ID	TCV AE (ml)	Cyst #1 (ml, (%))	Cyst #2 (ml, (%))	Cyst #3 (ml, (%))	Cyst #4 (ml, (%))	Cyst #5 (ml, (%))
Right kidney	1	78.90	15,41 (19.53)	12.04 (15.26)	8.49 (10.76)	4.76 (6.04)	3.51 (4.45)
	2	52.01	7.67 (14.75)	6.50 (12.49)	5.93 (11.40)	4.88 (9.39)	3.26 (6.27)
	3	121.96	50.36 (41.29)	12.81 (10.50)	10.89 (8.93)	10.53 (8.64)	9.70 (7.96)
	4	30.03	12.26 (40.81)	1.62 (5.40)	1.01 (3.37)	1.01 (3.36)	0.70 (2.33)
	5	160.07	23.93 (14.95)	21.71 (13.56)	20.17 (12.60)	13.18 (8.23)	7.16 (4.47)
Left kidney	1	34.91	7.54 (21.61)	3.36 (9.64)	2.86 (8.18)	2.44 (6.98)	2.07 (5.93)
	2	86.87	22.57 (25.98)	13.65 (15.72)	8.33 (9.59)	4.10 (4.73)	3.77 (4.34)
	3	164.65	43.34 (26.32)	38.92 (23.64)	12.52 (7.60)	11.13 (6.76)	7.36 (4.47)
	4	12.57	1.75 (13.93)	0.96 (7.64)	0.51 (4.03)	0.36 (2.88)	0.30 (2.42)
	5	129.65	18.14 (13.99)	14.80 (11.41)	10.30 (7.94)	10.21 (7.88)	8.73 (6.74)

Table 2.7: Volume and TCV percentage of the five biggest cysts for each kidney.

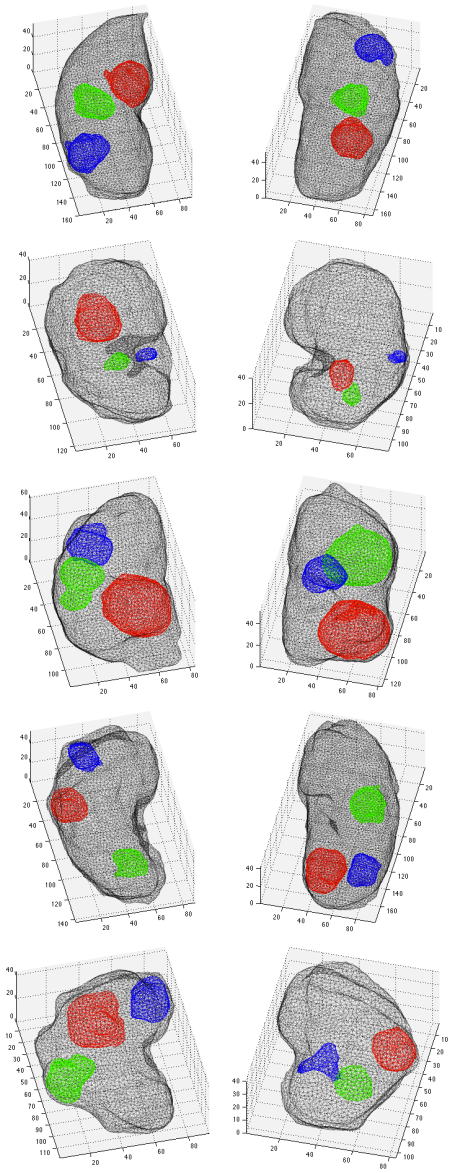

Figure 2.17: 3D representation of the three biggest cysts (in volume descendent order: red, green, blue) for left (left panels) and right (right panels) kidneys from patient 1 (top panels) to patient 5 (bottom panels).

2.4.3 Discussions

Total kidney volume is the common biomarker for the assessment of the polycystic disease. However TKV is computed in place of TCV since kidney enlargerment is mainly due to cyst expansion. The results presented in this study show as kidney with similar volume may have different residual parenchyma percentage (e. g. right kidney patient 2 versus right kidney patient 3, table 2.6) and so as TKV is not sufficient for assessing the progression of the disease. Furthermore, it is interesting to note that in some cases the two biggest cysts contribute to around half of TCV as shown in table 2.7 for right kidney of patient 3 and 4 and for left kidney of patient 3.

There are two phases of cystogenesis, an initial one gene-related and characterized by the development of cysts and a subsequent one, that is gene-independent and characterized by cyst enlargement [50]. The higher severity of PKD1 in comparison with PKD2 is due to number of cysts but not to the rate of cystic growth. The method that has been presented in this section can be an important instrument for the assessment of ADPKD progression as it provides quantitative informations about the number of cysts but also their volume and position, opening the possibility of new insight in the characterization of the ADPKD patient as for the detection of new possible clinical targets in the disease.

Chapter 3

Volumetric analysis in ADPKD patients from CT

Despite the drawbacks related to the use of ionizing radiation, computed tomagraphy is wildly used in clinical practice because it allows to acquire images faster than MRI and because of the widespread presence of CT scans in the territory. Early studies based on volumetric analysis of polycystic kidneys were performed on CT images but nowdays only few non manual approaches have been proposed for the assessment of kidney volume in PKD and all of them are based on contrast-enhanced CT images. In this chapter will be reviewed the recent methods that have been proposed in literature for the volumetric analysis in ADPKD patients from contrast-enhanced CT images and will be presented novel approaches for the automated assessment of kidney and cyst volume in ADPKD based on non-contrast-enhanced CT images.

3.1 State-of-the-art methods

3.1.1 Kidney segmentation in CT

Multiclass Otsu's thresholding approach

In a recent study [51], a new method for TKV/TCV estimation from CT was proposed which differs from the manual approach.
Initially, kidneys are manually outlined by an expert radiology or, in case of the absence of fat, segmented precisely to detect the area of interest. After this initialization, the following workflow is used for this algorithm:

- generation of binary mask from outlined images;
- application of the binary mask to a filtered version of the original images for image segmentation
- multiclass Otsu's thresholding approach [52], to distinguish cystic and parenchymal regions.

In the described method the authors used multislice CT in combination with non-ionic contrast agent.

Random forests approach

In this study [53] random forests classifier was trained and tested on 55 contrast enhanced CT images for kidney volume estimation. The different steps involved in this procedure are:

- computation of the intensity weighted geodesic distance based on manual segmentation of mid-slice;
- computation of a scalare feature value defining a box-feature based on pixel intensities;

- forest training and testing: different samples are selected 5 times so 44 samples are used for training and the remaining 11 for testing; training is performed two times, with and without the geodesic distance volume information.

3.2 Kidney and cyst volume estimation

The CRISP demonstrated that renal and cyst volume can be accurately and reliably measured in ADPKD using MR imaging techniques [43]. MR acquisition allows to overcome the limitation of CT such as the radiation exposure and the administration of contrast medium that can be nephrotoxic in patients with a decay in renal function [54]. In addition, MR images are able to provide more soft tissue details when compared with CT and for all these reasons, MRI is considered the best technique in clinical research. On the other hand, a CT examination costs generally less, takes less time and have higher resolution than MRI. Mainly because of the costs of an MRI system, small clinical centers, do not have MR scanners and, in clinical practice, CT imaging in ADPKD is very spread.
Despite the need and the continous progress made in the treatment of ADPKD patients, no automatic methods have been proposed for the estimation of TKV and TCV from CT images. As part of this Thesis, an automatic method for renal volume analysis from CT images has been developed and will be presented in the next sections. Importantly, no contrast medium was used during image acquisition.

3.2.1 Materials and methods

Eight ADPKD patients were involved in this study. For all patients ADPKD diagnostic was based on the Ultrasonographic Unified Criteria [23]. Patient characteristics are summerized in table 3.2. Images were acquired with a Siemens

Characteristic	Value
Number of patients	8
Sex (M/F)	4/4
Age at visit (years) **Mean ± SD** **[range]**	1797 ± 2171 [368 - 6794]
Total kidney volume (ml) **Mean ± SD[range]**	3528 ± 4375 [670 - 13727]
Left kidney volume (ml) **Mean ± SD[range]**	1731 ± 2212 [218 - 6933]
Right kidney volume (ml) **Mean ± SD[range]**	1797 ± 2171 [368 - 6794]

Table 3.1: Patient Characteristics.

Scope scan at the "Spedali Civili" of Brescia, Italy. Acquisition protocol is presented in table 3.1.

Tube voltage	130 KV
Tube current	37 mA
Matrix size	512x512 px
Pixel dimension	0.70 mm
Slice thickness	1.5 mm

Table 3.2: MRI protocol.

The proposed method has been developed for the detection of renal volume in ADPKD patients from CT images acquired without the use of contrast-medium (figure 3.1). It is fully-automated and the detection of kidneys contour is operated simultaneously for right and left kidneys. The workflow includes the pre-processing step, and the renal contour segmentation.

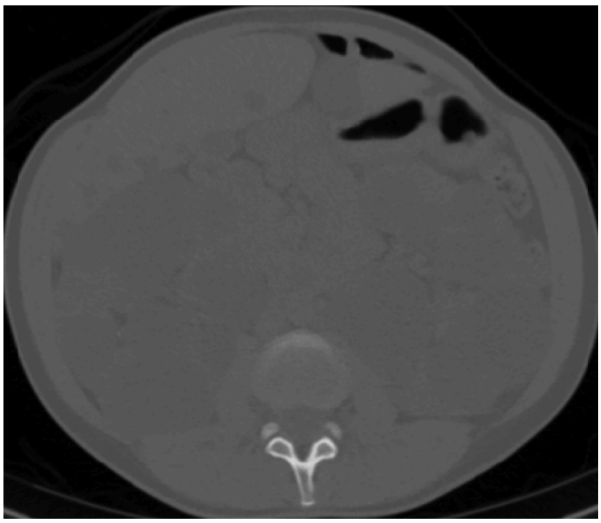

Figure 3.1: Original computed tomography image.

Kidney detection

CT images are characterized by low contrast (figure 3.1) which means that different tissues are represented with a few levels of gray and this is even more true in case of avoiding contrast agents. Because of that, different steps are involved for the localization of the kidneys.

Histogram analysis of the whole volume is performed in order to detect the range of pixel intensity in which the organs are included which is usually the last peak (figure 3.2, a). This allow to mask out bones and other structures that are not of interest and to facilitate the following unsupervised clustering which is based on pixel intensity information (figure 3.2, b). The whole volume is so clustered in four classes and the two ones with lower mean pixel intensity are taken in consideration. These classes tipically provide a rough segmentation of kidneys and cysts in the acquired volume. The distribution of the number of pixels associated to these classes in each slice of the acquired volume is then analyzed (figure 3.2, c). By selecting the maximum of this distribution, it can be identified the image plane with the the biggest kidney area which is generally

positioned around the middle of the whole renal volume. Once identified the the image plane the information provided by the clustering is used to detect the kidneys (figure 3.2, d).

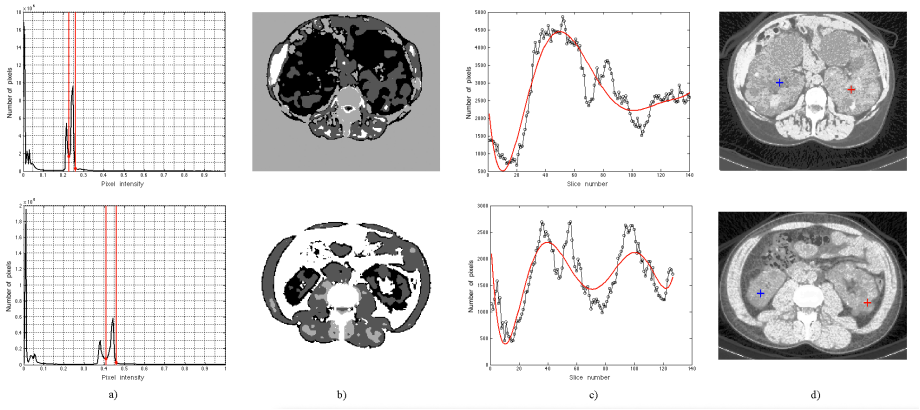

Figure 3.2: Description of the workflow for kidney detection on two different patients. (a) Histogram analyses of the 3d volume and detection of the pixel range; (b) Result of the 3d cluster in a single slice; (c) Number of pixel distribution associated to lowest pixel intensity; (d) Detection of the kidneys.

Renal contour segmentation

The information about the position of the kidneys is used for the initialization of a level set based segmentation. Before performing the segmentation the volume has been filtered using the non-local means approach. This kind of filter makes use of the information of all pixels in the image allowing to denoise the region while preserving its details. Multi-phase level set funtion is used for evolving a curve in the area of interest. This kind of level set approach comes in handy in presence of very large kidneys since it avoids to have overlapping areas. This approach makes the method suitable for the segmentation of kidney of different size and so of patient at different disease stage. Starting from the mid-slice this kind of segmentation is operated forward and backward in the remaining images. In each image, the level set is initialized based on the position of the

kidneys detected in the previous image.

Figure 3.3: Example of the detection of the renal regions in one patient.

3.2.2 Cyst detection

Beeing available the renal contouring and considering that in CT pixel intensity of cysts are lower respect to parenchyma, a three class clustering based on fuzzy c-means approach is used to outline the cystic area (figure 3.4). Similary to TKV, TCV is computed as the sum of the voxel count and considering the image resolution.

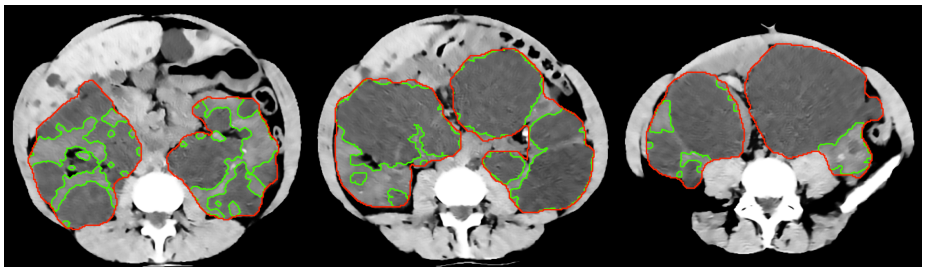

Figure 3.4: Example of the detection of renal and cystic regions in one patient.

3.2.3 Results

In this study one radiological reader manually traced the kidneys of each patient. Kidney volumes from automated and manual tracing were computed

multiplying the area of the renal contour of each image and the slice thickness. The agreement between the two methods were evaluated using linear regression analysis, Bland-Altman plots and dice similarity coefficient. Regression analysis (figure 3.5, top panel) showed a strong correlation between manual and automated volume estimation (r2 = 0.99; y = 0.99x-16.9). Bland-Altman analysis (figure 3.5, bottom panel) showed a low bias (-23.2 ml; -1.33%) and limits of agreements of 72.9 ml (4.2%). Absolute mean percentage error resulted in 6.2±4.8%. The reliability of this approach in terms of dice coefficient value was 0.91±0.03.

3.2.4 Discussion and conclusion

In this preliminary study it has been presented a novel fully automated method for ADPKD kidney segmentation on non contrast enhanced CT and showed how it is promising for facilitating kidney volume assessment. Cyst volume was excluded from the statistical analysis because in some kidney the parechyma was completely replaced by the cysts. TKV is recognized as the best biomarker for the evaluation of the progression of ADPKD disease. It has been proposed for ADPKD patient classification [42] and used for the evaluation of the progression of the disease in several clinical trials like [55, 15]. Despite the great interest of clinicians in the avalability of a method for polycystic kidney segmentation on CT, nowadays only two semi-automated approaches have been proposed [51, 53]. Both these methods use minimal user interaction and have been tested on contrast enhanced CT. Our method is no user dependent and it has been developed on non contrast enhanced CT and so avoiding the use of contrast medium. Further investigations will be necessary to properly assess the robustness of our method on a larger dataset.

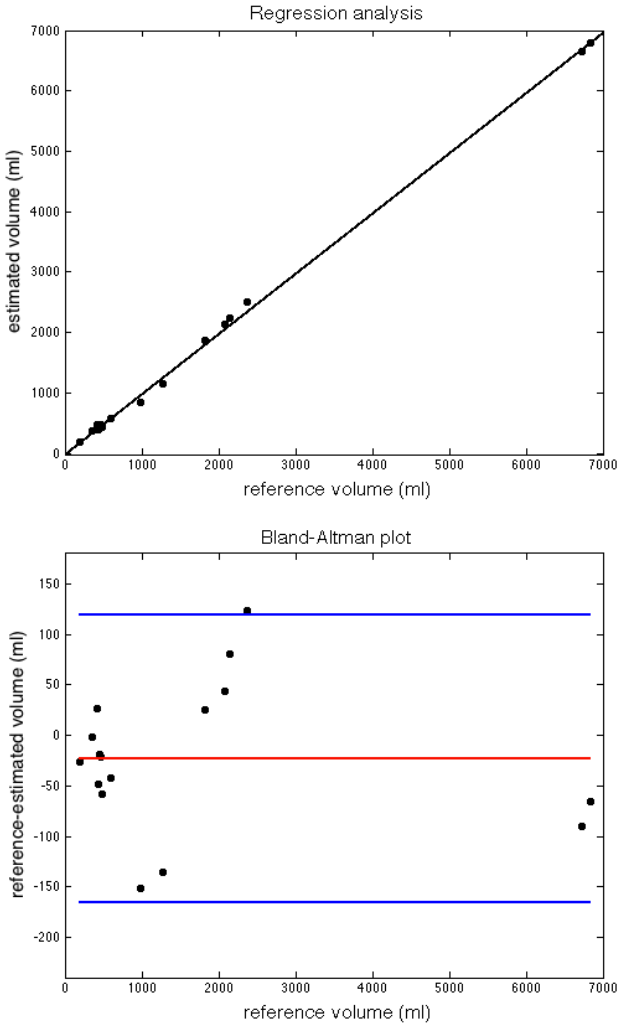

Figure 3.5: Linear regression (top panel) and Bland-Altmann (bottom panel) plots of the sixteen kidneys when compared to kidney volumes estimated from manual segmentation.

Chapter 4

Related projects

In this chapter two research projects focused on diffusion imaging in MRI are described. This innovative imaging technique which is commonly used in cerebral imaging could have important implications in different clinical scenarios including ADPKD and cancer patients.

The idea of investigating water motion can be exploited from different point of views and at different levels. Diffusion weighted imaging (DWI), diffusion tensor imaging (DTI) and intravoxel incoherent motion (IVIM) are three different approaches for providing different types of information for a functional characterization of a tissue trough the analysis of molecular diffusion of water and microcirculation of blood in the capillary network. Therefore in these two projects, that are strongly linked with the main research project developed in this Thesis, we investigate the potentiality of DWI, DTI and IVIM for providing functional information allowing to improve diagnosis and prognosis of ADPKD and cancer patients .

4.1 Diffusion tensor imaging of the kidney

This preliminary study was conducted to assess the feasibility of diffusion tensor imaging (DTI) for the characterization of cortex and medulla in an healthy population, as a first attempt to understand if DTI could be a useful for the evaluation of kidney function.

4.1.1 Diffusion tensor imaging

Diffusion-weighted imaging (DWI) is a non-invasive method for the analysis of the Brownian motion of water molecules in the extracellular space. Using DWI sequences, the apparent diffusion coefficient (ADC) can be measured. This quantitative parameter reflects cell density and microcirculation of the tissue allowing the evaluation of various abnormalities [56, 57, 58]. ADC is derived from the equation

$$ADC = -ln(S_i/S_0)/b$$

where b is the b value, S_i is the signal intensity of the image for a specific b value and diffusion gradient direction and S_0 is the signal intensity of the image without diffusion weighting.

ADC analysis is based on the assumption of free-molecular diffusion resulting in a too semplicistic model especially in the presence of organized structures in the tissue where the molecolar diffusion follows preferential directions. In the kidney, tubules, collecting ducts and vessels radially oriented towards the pelvis are responsible for diffusion anisotropy [59, 60].

Diffusion tensor imaging (DTI) is a particular MRI technique that allows the measurement of the degree of anisotropy and structural orientation in the tissue. The three-dimensional mechanisms of diffusion are described by the diffusion tensor. To quantify the degree of anisotropy, the diffusion model can be modeled by an ellipsoid represented by a tensor [61]. Eigenvalues of the diffusion tensor represent the principal diffusivities and are associated with three mutu-

ally perpendicular principal directions (eigenvectors). The tensor is represented by a 3 x 3 symmetric matrix:

$$D = \begin{bmatrix} D_{\mathrm{xx}} & D_{\mathrm{xy}} & D_{\mathrm{xz}} \\ D_{\mathrm{yx}} & D_{\mathrm{yy}} & D_{\mathrm{yz}} \\ D_{\mathrm{zx}} & D_{\mathrm{zy}} & D_{\mathrm{zz}} \end{bmatrix}$$

Being D_{xy}=D_{yx}, D_{xz}=D_{zx} and D_{yz}=D_{zy}, the tensor can be constructed using six diffusion-weighted images acquired along different directions. The diffusion tensor is calculated by solving the Stejskal-Tanner equation:

$$S_k = S_0 exp(-b g_k^T D g_k)$$

where S_k is the signal intensity when a gradient pulse is applied in the direction g_k, S_0 is the signal intensity measured with no diffusion-sensitizing gradient and b is a factor describing the pulse sequence, gradient strength, and physical constants [62, 63]. The equation represents the signal attenuation due to the application of a pulse gradient. In order to calculate the 6 independent components in the 3x3 symmetric matrix D, at least 7 images are needed: 6 diffusion-weighted images from 6 gradient directions (providing 6 values for S_k) plus one baseline image (giving $S0$). The previous equation can be expanded as follow:

$$-\frac{ln(\frac{S_k}{S_0})}{b} = (G_{xi}^2 D_{xx} + G_{yi}^2 D_{yy} + G_{zi}^2 D_{zz} + 2G_{xi}G_{yi}D_{xy} + 2G_{xi}G_{zi}D_{xz} 2G_{yi}G_{zi}D_{yz})$$

and solved as:

$$Y = Hd$$

where d is the column vector of D

$$d = [D_{xx}, D_{yy}, D_{zz}, D_{xy}, D_{xz}, D_{yz}]^T$$

H is a kx6 being k the number of gradient directions

$$H = \begin{bmatrix} G_{xx}^2 & G_{y1}^2 & G_{z1}^2 & 2G_{x1}G_{yi} & 2G_{xi}G_{z1} & 2G_{y1}G_{z1} \\ G_{x2}^2 & G_{y2}^2 & G_{z2}^2 & 2G_{x2}G_{y2} & 2G_{x2}G_{z2} & 2G_{y2}G_{z2} \\ \vdots & \vdots & \vdots & \vdots & \vdots & \vdots \\ G_{x6}^2 & G_{y6}^2 & G_{z6}^2 & 2G_{x6}G_{y6} & 2G_{x6}G_{z6} & 2G_{y6}G_{z6} \end{bmatrix}$$

and

$$Y = \left(\frac{ln(\frac{S_0}{S_1})}{b}, \frac{ln(\frac{S_0}{S_2})}{b}, \ldots, \frac{ln(\frac{S_0}{S_6})}{b} \right)$$

Then, diffusion tensor can be obtained considering:

$$(H^{-1}H)d = d = H^{-1}Y$$

Several scalar measurements can be obtained computing eigenvectors (e_1,e_2,e_3) and eigenvalues (λ_1,λ_2, λ_3) of the tensor from the diffusion tensor.
The mean diffusivity (MD) is a rotationally invariant measure of the magnitude of diffusion.

$$MD = \frac{\lambda_1 + \lambda_2 + \lambda_3}{3} = \frac{D_{xx} + D_{yy} + D_{zz}}{3}$$

The fractional anisotropy (FA) is a normalized measure of the fraction of the tensor's magnitude due to anisotropic diffusion

$$FA = \sqrt{\frac{(\lambda_1 - MD)^2 + (\lambda_2 - MD)^2 + (\lambda_3 - MD)^2}{2(\lambda_1^2 + \lambda_2^2 + \lambda_3^2)}}$$

The radial diffusivity (RD) is a measure of the diffusivity along the directions that are orthogonal to the principal one.

$$RD = (\lambda_2 + \lambda_3)/2$$

The volume ratio (VR) measures the ratio between the volume of the ellipsoid and the volume of a sphere of radius MD

$$VR = 1 - \frac{\lambda_1\lambda_2\lambda_3}{MD^3}$$

4.1.2 Image analysis

Ten subjects with age 33±12 and normal renal function estimated by GFR (mean 88 mL/min) with no history of renal disease, hypertension, diabetes or other vascular diseases underwent MRI. MRI images were obtained with a 1.5-T whole-body system (Signa HDxt; General Electric, Milwaukee, USA) and a standard phased-array body coil. The sequence was a spin-echo single-shot echo-planar imaging (SSEPI) acquired in the axial plane with breath hold. The MRI protocol is shown in table 4.1.

Repetition Time	3000 ms
Echo Time	82 ms
Field of view	40 cm
Slice thickness	6 mm
Gap	0.5 mm
Matrix size	128x128 px
Number of slices	14
b values	0 and 500 s/mm^2
Number of gradients	6

Table 4.1: MRI protocol

Regions of interest were manually defined in cortex and medulla of the kidneys of each patient and MD, FA, VR computed using the procedure previously described. A p-value <0.05 was considered statistically significant.

4.1.3 Results

In tables 4.2 and 4.3 the mean values obtained for the computed DTI parameters, for cortex and medulla respectively, are presented.

Parameter	Right kidney	Left kidney	p-value
MD ($x10^{-3}mm^2/s$)	2.70±0.36	2.68±0.31	0.77
FA	0.34±0.10	0.4±0.16	0.13
VR	0.15±0.1	0.21±0.16	0.14

Table 4.2: DTI parameters from renal cortex

Parameter	Right kidney	Left kidney	p-value
MD ($x10^{-3}mm^2/s$)	2.47±0.31	2.45±0.21	0.87
FA	0.36±0.09	0.47±0.14	0.01
VR	0.16±0.07	0.29±0.17	0.02

Table 4.3: DTI parameters from renal medulla

4.1.4 Discussion

Mean values of the DTI parameters are in line with those published in recent studies [60]. The results show also a significative difference in FA (p=0.01) and VR (p=0.02) in renal medulla, between left and right kidney. This difference may be due to a functional or structural difference in the kidneys. Similar difference was found in [64]. A larger study population is needed for confirming and better investigate this matter.

4.2 Diffusion-weighted MRI in the assessment of ADPKD disease

In this preliminary study we investigated the feasibility of functional parameters derived from DWI analysis for providing therapeutic indication for patients in the first stages of the disease or surgical indications and check for those patients with end-stage chronical disease that are candidates for nephrectomy. This is part of an ongoing collaboration between the University of Bologna

and the Ospedale Sant'Orsola of Bologna (Italy) which involves bioingineers, nefrologists, radiologists and pathologists.

4.2.1 Case of study

The first case of study was an ADPKD patient candidate for nephrectomy. For this 42 years old female patient, the removal of the organ was required because she was suffering a great deal of pain and the enlargement of the kidneys caused an important burden in the abdomen.

4.2.2 In-vivo and ex-vivo analysis

Before surgery, morphological and functional MR images of the abdomen were acquired.

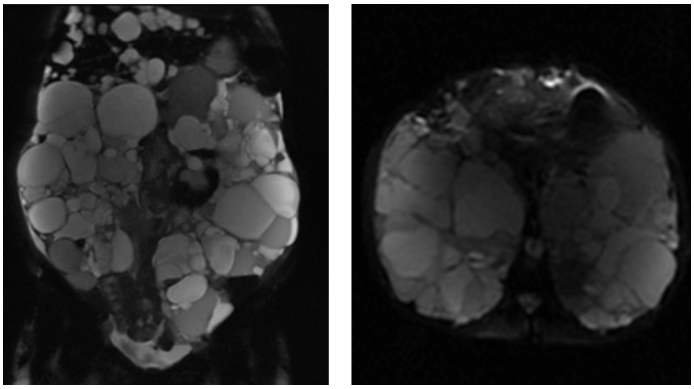

Figure 4.1: Two images in coronal (left panel) and axial (right panel) views of the kidneys.

T2-weighted and diffusion-weighted images (figure 4.1) were acquired.
After surgery, the volume of the explanted polycystic kidney (figure 4.2) was estimated through Archimede's principle and resulted in about 5000 ml. Ultrasound analysis was performed in order to investigate the possibility of the

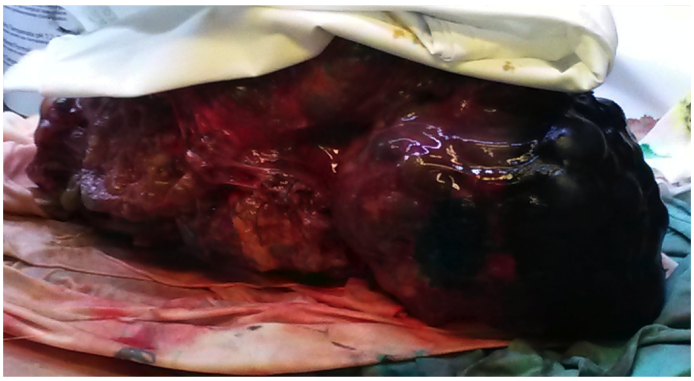

Figure 4.2: A picture of the explanted kidney.

Figure 4.3: Anatomical specimens of the explanted kidney before formaline filling.

presence of residual parenchyma. Renal cyst fluid was aspired by the pathologist from those cysts positioned in the exterior part of the kidney and that could be easily identified in the MR images. The kidney was then dissectioned and several specimens extracted (figure 4.3).

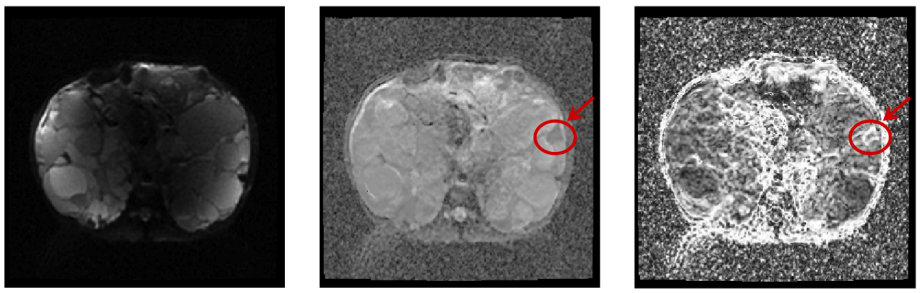

Figure 4.4: From left to right: S_0, MD map, FA map

4.2.3 Results

Kidney volume was estimated via manual contour and using the semi-automatic method described in the previous chapter and resulted in 5120 ml and 4962 ml, variating from the empirical estimation of +2.5% and -0.76% respectively.
Mean diffusivity, fractional anisotropy and radial diffusivity were measured from DWI data, highlighting the presence of normal parenchyma (figure 4.4). No normal parenchyma was detected using ultrasounds. Histological analysis showed the presence of extended fibrosis but also 30% of normal tissue in the renal specimens examined.

4.2.4 Discussion

Volume analysis allowed an in vivo validation of the semi-automated approach for TKV computation. Surprisingly, histological examination confirmed the presence of normal parenchimal tissue, which was not expected since morphological images showed that renal parenchyma was completely replaced by cysts. Ultrasound appears to be not suitable for detecting any kind of parenchyma in kidney with so many cysts. This study on a single patient represents a proof of concept of the potential utility of using informations extracted from diffusion tensor imaging for evaluating the presence of normal parenchyma. Actually, histological analysis is the only technique available for this kind of analysis and

the use of diffusion images may be aof value for providing additional functional information applying a non invasive approach.

4.3 IVIM analysis of breast lesions

The expertise gained in the analysis of functional images was extended to the study of breast lesions from intravoxel incoherent motion (IVIM) and dynamic contrast-enhanced (DCE) MRI. In this study, perfusion and diffusion MRI metrics have been computed and analysed for the evaluation of breast lesions.

4.3.1 Introduction

Cancer is characterized by a high biological heterogeneity [65, 66, 67]. Such heterogeneity has been confirmed in particular for breast cancer [68]. In this contex, the avalability of biomarkers for quantitative analysis and differentiation of lesions has become critical.

Conventional mammography is the most common modality for screening breast cancer but has shown low sensitivity in particular in cases of dense breast parenchyma [69]. In comparison with mammography, contrast-enhanced MRI allows to study tissue perfusion by a quantitative analysis of pharmacokinetic parameters showing high sensitivity but low specificity [70]. Recently, a lot of interest has been put in DWI analysis for the differentiation between benign and malign lesions. Furthermore, DWI acquisitions do not require the use of contrast medium and it has been seen that DWI parameters such as the apparent diffusion coefficient (ADC) is able to differentiate breast lesions [71]. However, the sensitivity and specificity among different studies can vary a lot [71, 72, 73] also because of the choise of different maximum b-values that can lead to an overestimation of ADC [74]. IVIM technique makes use of multi b-value DWI and is able to provide separated information about perfusion and diffusion [75]. Nowadays only few studies have explored the capability of this technique in the

differetiation of breast lesions but the preliminary results are promising. Aim of this study was to evaluate the diagnostic potential of IVIM and DCE for breast lesions.

4.3.2 Image analysis

ADC maps were obtained assuming the monoexponential model for diffusion-weighted images at all b-values:

$$S(b) = S_0 exp(-bADC)$$

where b is the b-value and S_0 and $S(b)$ denote the signal intensity of diffusion-weighted images acquired with b-value of zero and b respectively.

To compute the IVIM parameters was used the biexponetial model as described by Bihan [75] :

$$S(b) = S_0[(1-f)exp(-bD) + fexp(-b(D+D*)]$$

where f is the perfusion fraction representing the microvasculare volume fraction, D is the true coefficient representing the pure water molecular diffusion and $D*$ is the pseudodiffusion coefficient representing which reflects the perfusion-related diffusion (incoherent microcirculation). Several calculation methods have been proposed for the computation of these parameters and among them there are [76, 77, 78]. In this study, considering the relatively few number of b-values, it was used the segmented approach [76] which is also considered more robust than the simultaneous full fitting [79, 80].
The segmented approach is based on the assumption that being $D*$ greater then D its effects on the signal decay at large b is negligible. D is determined from data within on interval of high b-values (b >200 s/mm^2) using the least squares curve fit:

$$S_{\text{high}}(b) = S_{\text{high0}}(1-f)exp(-bD)$$

where $S_{\text{high0}} = S_0(1-f)$. Then f is determined from S_0 as $f = (S_0 - S_{\text{high0}})/S_0$. Finally $D*$ is obtained from the monoexponential fit using the precalculated D and f. The goodness of the fit was evaluated using the R^2 value:

$$R^2 = 1 - SSE/TSS$$

where SSE is the sum of squared erros between the data and the fitting curve and TSS is the sum of squared differences between the data and the mean of all data values. Voxels with R^2 value above 0.8 were excluded from the analysis. For each detected lesion, and for each parametrical map, as in was computed: Quantitative analysis of ADC, f, D, $D*$ included: mean and standard deviation, median and quartiles, total numer of voxel included in the analysis, total numer of voxel excluded from the analysis, skewness, kurtosis, contrast, correlation, energy, homogeneity.

DCE analysis was performed constructing a time intensity curve (TIC) for each detected lesion. Quantitative analysis included: wash-in slope, wash-out slope, absolute percentage enhancement, time to maximum enhancement, contrast, correlation, energy, homogeneity.

In figure 4.5 is illustrated the interface developed for IVIM and DCE analysis from MRI.

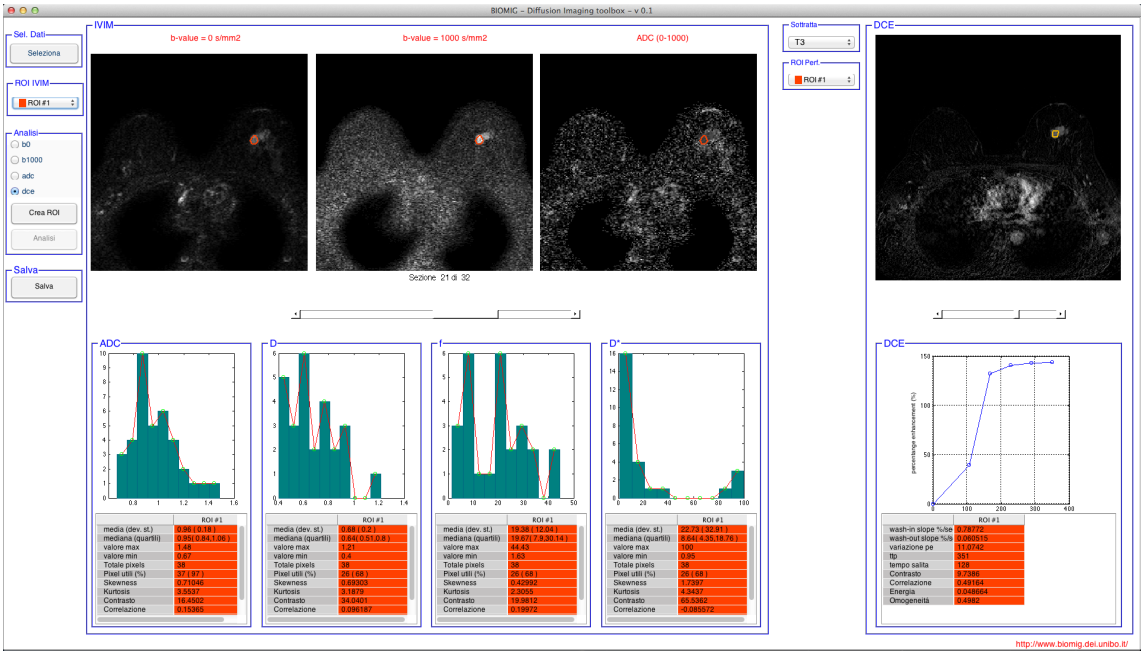

Figure 4.5: Interface for IVIM and DCE analysis from MRI

Bibliography

[1] Zhiguo Mao, Jiehan Chong, and Albert CM Ong. Autosomal dominant polycystic kidney disease: recent advances in clinical management. *F1000Research*, 5, 2016.

[2] Peter C Harris and Vicente E Torres. Polycystic kidney disease. *Annual review of medicine*, 60:321, 2009.

[3] Amirali Masoumi, Berenice Reed-Gitomer, Catherine Kelleher, Mir Reza Bekheirnia, and Robert W Schrier. Developments in the management of autosomal dominant polycystic kidney disease. *Therapeutics and clinical risk management*, 4(2):393, 2008.

[4] Albert CM Ong, Olivier Devuyst, Bertrand Knebelmann, Gerd Walz, and ERA-EDTA Working Group for Inherited. Autosomal dominant polycystic kidney disease: the changing face of clinical management. *The Lancet*, 385(9981):1993–2002, 2015.

[5] Véronique Chauvet, Feng Qian, Nicolas Boute, Yiqiang Cai, Bunyong Phakdeekitacharoen, Luis F Onuchic, Tania Attié-Bitach, Liliane Guicharnaud, Olivier Devuyst, Gregory G Germino, et al. Expression of pkd1 and pkd2 transcripts and proteins in human embryo and during normal kidney development. *The American journal of pathology*, 160(3):973–983, 2002.

[6] Moumita Barua and York Pei. Diagnosis of autosomal-dominant polycystic kidney disease: an integrated approach. 30(4):356–365, 2010.

[7] Vicente E Torres, Peter C Harris, and Yves Pirson. Autosomal dominant polycystic kidney disease. *The Lancet*, 369(9569):1287–1301, 2007.

[8] Imed Helal, Berenice Reed, and Robert W Schrier. Emergent early markers of renal progression in autosomal-dominant polycystic kidney disease patients: implications for prevention and treatment. *American journal of nephrology*, 36(2):162–167, 2012.

[9] Cristian Riella, Peter G Czarnecki, and Theodore I Steinman. Therapeutic advances in the treatment of polycystic kidney disease. *Nephron Clinical Practice*, 128(3-4):297–302, 2015.

[10] SL Alan, Mireille El-Ters, and Franz T Winklhofer. Clinical trials in autosomal dominant polycystic kidney disease. 2015.

[11] Patricia A Gabow, Arlene B Chapman, Ann M Johnson, Douglas J Tangel, Irene T Duley, William D Kaehny, Michael Manco-Johnson, and Robert W Schrier. Renal structure and hypertension in autosomal dominant polycystic kidney disease. *Kidney international*, 38(6):1177–1180, 1990.

[12] Arlene B Chapman, Konrad Stepniakowski, and Frederic Rahbari-Oskoui. Hypertension in autosomal dominant polycystic kidney disease. *Advances in chronic kidney disease*, 17(2):153–163, 2010.

[13] Xiaofang Wang, Vincent Gattone, Peter C Harris, and Vicente E Torres. Effectiveness of vasopressin v2 receptor antagonists opc-31260 and opc-41061 on polycystic kidney disease development in the pck rat. *Journal of the American Society of Nephrology*, 16(4):846–851, 2005.

[14] Vicente E Torres, Arlene B Chapman, Olivier Devuyst, Ron T Gansevoort, Jared J Grantham, Eiji Higashihara, Ronald D Perrone, Holly B Krasa, John Ouyang, and Frank S Czerwiec. Tolvaptan in patients with autosomal dominant polycystic kidney disease. *New England Journal of Medicine*, 367(25):2407–2418, 2012.

[15] Anna Caroli, Norberto Perico, Annalisa Perna, Luca Antiga, Paolo Brambilla, Antonio Pisani, Bianca Visciano, Massimo Imbriaco, Piergiorgio Messa, Roberta Cerutti, et al. Effect of longacting somatostatin analogue on kidney and cyst growth in autosomal dominant polycystic kidney disease (aladin): a randomised, placebo-controlled, multicentre trial. *The Lancet*, 382(9903):1485–1495, 2013.

[16] Gerd Walz, Klemens Budde, Marwan Mannaa, Jens Nürnberger, Christoph Wanner, Claudia Sommerer, Ulrich Kunzendorf, Bernhard Banas, Walter H Hörl, Nicholas Obermüller, et al. Everolimus in patients with autosomal dominant polycystic kidney disease. *New England Journal of Medicine*, 363(9):830–840, 2010.

[17] Andreas L Serra, Diane Poster, Andreas D Kistler, Fabienne Krauer, Shagun Raina, James Young, Katharina M Rentsch, Katharina S Spanaus, Oliver Senn, Paulus Kristanto, et al. Sirolimus and kidney growth in autosomal dominant polycystic kidney disease. *New England Journal of Medicine*, 363(9):820–829, 2010.

[18] G Canaud, B Knebelmann, Peter C Harris, F Vrtovsnik, J-M Correas, N Pallet, CM Heyer, E Letavernier, F Bienaime, E Thervet, et al. Therapeutic mtor inhibition in autosomal dominant polycystic kidney disease: What is the appropriate serum level? *American Journal of Transplantation*, 10(7):1701–1706, 2010.

[19] Maria V Irazabal and Vicente E Torres. Experimental therapies and ongoing clinical trials to slow down progression of adpkd. *Current hypertension reviews*, 9(1):44–59, 2013.

[20] Sandro Rossetti, Mark B Consugar, Arlene B Chapman, Vicente E Torres, Lisa M Guay-Woodford, Jared J Grantham, William M Bennett, Catherine M Meyers, Denise L Walker, Kyongtae Bae, et al. Comprehensive molecular diagnostics in autosomal dominant polycystic kidney disease. *Journal of the American Society of Nephrology*, 18(7):2143–2160, 2007.

[21] Sanem Guler, Sertac Cimen, Scott Hurton, and Michele Molinari. Diagnosis and treatment modalities of symptomatic polycystic kidney disease.

[22] D Ravine, LJ Sheffield, DM Danks, RN Gibson, RG Walker, and P Kincaid-Smith. Evaluation of ultrasonographic diagnostic criteria for autosomal dominant polycystic kidney disease 1. *The Lancet*, 343(8901):824–827, 1994.

[23] York Pei, James Obaji, Annie Dupuis, Andrew D Paterson, Riccardo Magistroni, Elizabeth Dicks, Patrick Parfrey, Benvon Cramer, Eliecer Coto, Roser Torra, et al. Unified criteria for ultrasonographic diagnosis of adpkd. *Journal of the American Society of Nephrology*, 20(1):205–212, 2009.

[24] Wojciech Wołyniec, Magdalena Maria Jankowska, Ewa Król, Piotr Czarniak, and Bolesław Rutkowski. Current diagnostic evaluation of autosomal dominant polycystic kidney disease. *Pol Arch Med Wewn*, 118(12):767–73, 2008.

[25] Arlene B Chapman and Wenjing Wei. Imaging approaches to patients with polycystic kidney disease. 31(3):237–244, 2011.

[26] Jeannette Bakker, Marco Olree, Robert Kaatee, Eduard E de Lange, Karel GM Moons, Jaap J Beutler, and Frederik JA Beek. Renal volume measurements: accuracy and repeatability of us compared with that of mr imaging 1. *Radiology*, 211(3):623–628, 1999.

[27] Henrik S Thomsen, Jan Kyst Madsen, Jørn Hess Thaysen, and Karen Damgaard-Petersen. Volume of polycystic kidneys during reduction of renal function. *Urologic radiology*, 3(2):85–89, 1981.

[28] Lilach O Lerman, MICHAEL D BENTLEY, MALCOLM R BELL, JOHN A RUMBERGER, and J CARLOS ROMERO. Quantitation of the in vivo kidney volume with cine computed tomography. *Investigative radiology*, 25(11):1206–1211, 1990.

[29] CJ Kotre and JP Owen. Method for the evaluation of renal parenchymal volume by x-ray computed tomography. *Medical and Biological Engineering and Computing*, 32(3):338–341, 1994.

[30] Bernard F King, Judd E Reed, Erik J Bergstralh, Patrick F Sheedy, and Vicente E Torres. Quantification and longitudinal trends of kidney, renal cyst, and renal parenchyma volumes in autosomal dominant polycystic kidney disease. *Journal of the American Society of Nephrology*, 11(8):1505–1511, 2000.

[31] Cori Sise, Masatomo Kusaka, Louis H Wetzel, Franz Winklhofer, Benjamin D Cowley, Larry T Cook, Michael Gordon, and Jared J Grantham. Volumetric determination of progression in autosomal dominant polycystic kidney disease by computed tomography. *Kidney international*, 58(6):2492–2501, 2000.

[32] Kyongtae T Bae, Cheng Tao, Jinhong Wang, Diana Kaya, Zhiyuan Wu, Junu T Bae, Arlene B Chapman, Vicente E Torres, Jared J Grantham, Michal Mrug, et al. Novel approach to estimate kidney and cyst volumes using mid-slice magnetic resonance images in polycystic kidney disease. *American journal of nephrology*, 38(4):333–341, 2013.

[33] Timothy L Kline, Panagiotis Korfiatis, Marie E Edwards, Joshua D Warner, Maria V Irazabal, Bernard F King, Vicente E Torres, and Bradley J Erickson. Automatic total kidney volume measurement on follow-up magnetic resonance images to facilitate monitoring of autosomal dominant polycystic kidney disease progression. *Nephrology Dialysis Transplantation*, page gfv314, 2015.

[34] Youngwoo Kim, Yinghui Ge, Cheng Tao, Jianbing Zhu, Arlene B Chapman, Vicente E Torres, SL Alan, Michal Mrug, William M Bennett, Michael F Flessner, et al. Automated segmentation of kidneys from mr images in patients with autosomal dominant polycystic kidney disease. *Clinical Journal of the American Society of Nephrology*, 11(4):576–584, 2016.

[35] Kyongtae T Bae, Paul K Commean, and Jeongrim Lee. Volumetric measurement of renal cysts and parenchyma using mri: phantoms and patients with polycystic kidney disease. *Journal of computer assisted tomography*, 24(4):614–619, 2000.

[36] Kyungsoo Bae, Bumwoo Park, Hongliang Sun, Jinhong Wang, Cheng Tao, Arlene B Chapman, Vicente E Torres, Jared J Grantham, Michal Mrug, William M Bennett, et al. Segmentation of individual renal cysts from mr images in patients with autosomal dominant polycystic kidney disease. *Clinical Journal of the American Society of Nephrology*, 8(7):1089–1097, 2013.

[37] Kyongtae T Bae, Hongliang Sun, June Goo Lee, Kyungsoo Bae, Jinhong Wang, Cheng Tao, Arlene B Chapman, Vicente E Torres, Jared J Grantham, Michal Mrug, et al. Novel methodology to evaluate renal cysts in polycystic kidney disease. *American journal of nephrology*, 39(3):210–217, 2014.

[38] Renzo Mignani, Cristiana Corsi, Mariangela De Marco, Enrico G Caiani, Gioele Santucci, Enrico Cavagna, Stefano Severi, and Leonardo Cagnoli. Assessment of kidney volume in polycystic kidney disease using magnetic resonance imaging without contrast medium. *American journal of nephrology*, 33(2):176–184, 2011.

[39] Dario Turco, Stefano Severi, Renzo Mignani, Valeria Aiello, Riccardo Magistroni, and Cristiana Corsi. Reliability of total renal volume computation in polycystic kidney disease from magnetic resonance imaging. *Academic radiology*, 22(11):1376–1384, 2015.

[40] Benjamin A Cohen, Irina Barash, Danny C Kim, Matthew D Sanger, James S Babb, and Hersh Chandarana. Intraobserver and interobserver variability of renal volume measurements in polycystic kidney disease using a semiautomated mr segmentation algorithm. *American Journal of Roentgenology*, 199(2):387–393, 2012.

[41] Jared J Grantham and Vicente E Torres. The importance of total kidney volume in evaluating progression of polycystic kidney disease. *Nature Reviews Nephrology*, 2016.

[42] María V Irazabal, Laureano J Rangel, Eric J Bergstralh, Sara L Osborn, Amber J Harmon, Jamie L Sundsbak, Kyongtae T Bae, Arlene B Chapman, Jared J Grantham, Michal Mrug, et al. Imaging classification of autosomal dominant polycystic kidney disease: a simple model for selecting patients for clinical trials. *Journal of the American Society of Nephrology*, 26(1):160–172, 2015.

[43] Arlene B Chapman, Lisa M Guay-Woodford, Jared J Grantham, Vicente E Torres, Kyongtae T Bae, Deborah A Baumgarten, Philip J Kenney, Bernard F King, James F Glockner, Louis H Wetzel, et al. Renal structure in early autosomal-dominant polycystic kidney disease (adpkd): The consortium for radiologic imaging studies of polycystic kidney disease (crisp) cohort. *Kidney international*, 64(3):1035–1045, 2003.

[44] W Charles O'Neill, Michelle L Robbin, Kyongtae T Bae, Jared J Grantham, Arlene B Chapman, Lisa M Guay-Woodford, Vicente E Torres, Bernard F King, Louis H Wetzel, Paul A Thompson, et al. Sonographic assessment of the severity and progression of autosomal dominant polycystic kidney disease: the consortium of renal imaging studies in polycystic kidney disease (crisp). *American journal of kidney diseases*, 46(6):1058–1064, 2005.

[45] Edwin M Spithoven, Maatje DA van Gastel, A Lianne Messchendorp, Niek F Casteleijn, Joost PH Drenth, Carlo A Gaillard, Johan W de Fijter, Esther Meijer, Dorien JM Peters, Peter Kappert, et al. Estimation of total kidney volume in autosomal dominant polycystic kidney disease. *American Journal of Kidney Diseases*, 66(5):792–801, 2015.

[46] Harpreet Bhutani, Vikram Smith, Frederic Rahbari-Oskoui, Ankush Mittal, Jared J Grantham, Vicente E Torres, Michal Mrug, Kyongtae T Bae, Zhiyuan Wu, Yinghui Ge, et al. A comparison of ultrasound and mag-

netic resonance imaging shows that kidney length predicts chronic kidney disease in autosomal dominant polycystic kidney disease. *Kidney international*, 88(1):146–151, 2015.

[47] Maria V Irazabal, Jaime D Blais, Ronald D Perrone, Ron T Gansevoort, Arlene B Chapman, Olivier Devuyst, Eiji Higashihara, Peter C Harris, Wen Zhou, John Ouyang, et al. Prognostic enrichment design in clinical trials for autosomal dominant polycystic kidney disease: The tempo 3: 4 clinical trial. *Kidney International Reports*, 1(4):213–220, 2016.

[48] Xin Qi, Fuyong Xing, David J Foran, and Lin Yang. Robust segmentation of overlapping cells in histopathology specimens using parallel seed detection and repulsive level set. *IEEE Transactions on Biomedical Engineering*, 59(3):754–765, 2012.

[49] Bahram Parvin, Qing Yang, Ju Han, Hang Chang, Bjorn Rydberg, and Mary Helen Barcellos-Hoff. Iterative voting for inference of structural saliency and characterization of subcellular events. *IEEE Transactions on Image Processing*, 16(3):615–623, 2007.

[50] Peter C Harris, Kyongtae T Bae, Sandro Rossetti, Vicente E Torres, Jared J Grantham, Arlene B Chapman, Lisa M Guay-Woodford, Bernard F King, Louis H Wetzel, Deborah A Baumgarten, et al. Cyst number but not the rate of cystic growth is associated with the mutated gene in autosomal dominant polycystic kidney disease. *Journal of the American Society of Nephrology*, 17(11):3013–3019, 2006.

[51] Luca Antiga, Marina Piccinelli, Giorgio Fasolini, Bogdan Ene-Iordache, Patrizia Ondei, Simona Bruno, Giuseppe Remuzzi, and Andrea Remuzzi. Computed tomography evaluation of autosomal dominant polycystic kidney disease progression: a progress report. *Clinical Journal of the American Society of Nephrology*, 1(4):754–760, 2006.

[52] Nobuyuki Otsu. A threshold selection method from gray-level histograms. *Automatica*, 11(285-296):23–27, 1975.

[53] Kanishka Sharma, Loic Peter, Christian Rupprecht, Anna Caroli, Lichao Wang, Andrea Remuzzi, Maximilian Baust, and Nassir Navab. Semi-automatic segmentation of autosomal dominant polycystic kidneys using random forests. *arXiv preprint arXiv:1510.06915*, 2015.

[54] Hitoshi Katayama, K Yamaguchi, T Kozuka, T Takashima, P Seez, and K Matsuura. Adverse reactions to ionic and nonionic contrast media. a report from the japanese committee on the safety of contrast media. *Radiology*, 175(3):621–628, 1990.

[55] Vicente E Torres, Esther Meijer, Kyongtae T Bae, Arlene B Chapman, Olivier Devuyst, Ron T Gansevoort, Jared J Grantham, Eiji Higashihara, Ronald D Perrone, Holly B Krasa, et al. Rationale and design of the tempo (tolvaptan efficacy and safety in management of autosomal dominant polycystic kidney disease and its outcomes) 3-4 study. *American journal of kidney diseases*, 57(5):692–699, 2011.

[56] DM Koh and AR Padhani. Diffusion-weighted mri: a new functional clinical technique for tumour imaging. *The British Journal of Radiology*, 2014.

[57] A Kido, Masako Kataoka, T Koyama, A Yamamoto, Tsuneo Saga, and K Togashi. Changes in apparent diffusion coefficients in the normal uterus during different phases of the menstrual cycle. *The British journal of radiology*, 2014.

[58] Xueqin Xu, Wenqiang Fang, Huawei Ling, Weimin Chai, and Kemin Chen. Diffusion-weighted mr imaging of kidneys in patients with chronic kidney disease: initial study. *European radiology*, 20(4):978–983, 2010.

[59] Mario Ries, Richard A Jones, Fabrice Basseau, Chrit TW Moonen, and Nicolas Grenier. Diffusion tensor mri of the human kidney. *Journal of Magnetic Resonance Imaging*, 14(1):42–49, 2001.

[60] Caterina Gaudiano, Valeria Clementi, Fiorenza Busato, Beniamino Corcioni, Maria Grazia Orrei, Emiliana Ferramosca, Emma Fabbri, Paola Be-

rardi, Antonio Santoro, and Rita Golfieri. Diffusion tensor imaging and tractography of the kidneys: assessment of chronic parenchymal diseases. *European radiology*, 23(6):1678–1685, 2013.

[61] Peter J Basser, James Mattiello, and Denis LeBihan. Estimation of the effective self-diffusion tensor from the nmr spin echo. *Journal of Magnetic Resonance, Series B*, 103(3):247–254, 1994.

[62] Denis Le Bihan and Peter J Basser. Molecular diffusion and nuclear magnetic resonance. *Diffusion and perfusion magnetic resonance imaging*, pages 5–17, 1995.

[63] Lauren J O'Donnell and Carl-Fredrik Westin. An introduction to diffusion tensor image analysis. *Neurosurgery clinics of North America*, 22(2):185–196, 2011.

[64] Zhenfeng Zheng, Huilan Shi, Jing Zhang, and Yunting Zhang. Renal water molecular diffusion characteristics in healthy native kidneys: assessment with diffusion tensor mr imaging. *PloS one*, 9(12):e113469, 2014.

[65] I What. Tumor heterogeneity. *Cancer research*, 44:2259–2265, 1984.

[66] Corbin E Meacham and Sean J Morrison. Tumour heterogeneity and cancer cell plasticity. *Nature*, 501(7467):328–337, 2013.

[67] Philippe L Bedard, Aaron R Hansen, Mark J Ratain, and Lillian L Siu. Tumour heterogeneity in the clinic. *Nature*, 501(7467):355–364, 2013.

[68] Kornelia Polyak. Heterogeneity in breast cancer. *The Journal of clinical investigation*, 121(10):3786–3788, 2011.

[69] Denise R Aberle, Caroline Chiles, Constanine Gatsonis, Bruce J Hillman, C Daniel Johnson, Bruce L McClennan, Donald G Mitchell, Etta D Pisano, Mitchell D Schnall, and A Gregory Sorensen. Imaging and cancer: Research strategy of the american college of radiology imaging network 1. *Radiology*, 235(3):741–751, 2005.

[70] Nicky HGM Peters, Inne HM Borel Rinkes, Nicolaas PA Zuithoff, Willem PTM Mali, Karel GM Moons, and Petra HM Peeters. Meta-analysis of mr imaging in the diagnosis of breast lesions 1. *Radiology*, 246(1):116–124, 2008.

[71] Savannah C Partridge, Wendy B DeMartini, Brenda F Kurland, Peter R Eby, Steven W White, and Constance D Lehman. Differential diagnosis of mammographically and clinically occult breast lesions on diffusion-weighted mri. *Journal of Magnetic Resonance Imaging*, 31(3):562–570, 2010.

[72] Riham H EI Khouli, Michael A Jacobs, Sarah D Mezban, Peng Huang, Ihab R Kamel, Katarzyna J Macura, and David A Bluemke. Diffusion-weighted imaging improves the diagnostic accuracy of conventional 3.0-t breast mr imaging 1. *Radiology*, 256(1):64–73, 2010.

[73] Sibel Kul, Aysegul Cansu, Etem Alhan, Hasan Dinc, Gurbuz Gunes, and Abdulkadir Reis. Contribution of diffusion-weighted imaging to dynamic contrast-enhanced mri in the characterization of breast tumors. *American Journal of Roentgenology*, 196(1):210–217, 2011.

[74] Chunling Liu, Kun Wang, Queenie Chan, Zaiyi Liu, Jine Zhang, Hui He, Shuixing Zhang, and Changhong Liang. Intravoxel incoherent motion mr imaging for breast lesions: comparison and correlation with pharmacokinetic evaluation from dynamic contrast-enhanced mr imaging. *European radiology*, pages 1–11, 2016.

[75] Denis Le Bihan, Eric Breton, Denis Lallemand, Philippe Grenier, Emmanuel Cabanis, and Maurice Laval-Jeantet. Mr imaging of intravoxel incoherent motions: application to diffusion and perfusion in neurologic disorders. *Radiology*, 161(2):401–407, 1986.

[76] EE Sigmund, GY Cho, S Kim, M Finn, M Moccaldi, JH Jensen, DK Sodickson, JD Goldberg, S Formenti, and L Moy. Intravoxel incoherent motion imaging of tumor microenvironment in locally advanced breast cancer. *Magnetic resonance in medicine*, 65(5):1437–1447, 2011.

[77] Mami Iima, Masako Kataoka, Denis Le Bihan, Masaki Umehana, Takuma Imakita, Masayuki Nakagawa, Shotaro Kanao, Kojiro Yano, Thorsten Feiweier, and Kaori Togashi. Potential of perfusion imaging with ivim mri in breast cancer. In *Proceedings of the 21st Annual Meeting of ISMRM, Salt Lake City*, 2013.

[78] Line B Nilsen, Anne Fangberget, Oliver Geier, and Therese Seierstad. Quantitative analysis of diffusion-weighted magnetic resonance imaging in malignant breast lesions using different b value combinations. *European radiology*, 23(4):1027–1033, 2013.

[79] Gene Young Cho, Linda Moy, Jeff L Zhang, Steven Baete, Riccardo Lattanzi, Melanie Moccaldi, James S Babb, Sungheon Kim, Daniel K Sodickson, and Eric E Sigmund. Comparison of fitting methods and b-value sampling strategies for intravoxel incoherent motion in breast cancer. *Magnetic resonance in medicine*, 74(4):1077–1085, 2015.

[80] Shiteng Suo, Naier Lin, He Wang, Liangbin Zhang, Rui Wang, Su Zhang, Jia Hua, and Jianrong Xu. Intravoxel incoherent motion diffusion-weighted mr imaging of breast cancer at 3.0 tesla: Comparison of different curve-fitting methods. *Journal of Magnetic Resonance Imaging*, 42(2):362–370, 2015.